Ore Geology Reviews 137 (2021) 104271

Contents lists available at ScienceDirect

Ore Geology Reviews

journal homepage: www.elsevier.com/locate/oregeorev

Mapping lithological units, structural lineaments and alteration zones in the Southern Kibi-Winneba belt of Ghana using integrated geophysical and remote sensing datasets

Eric Dominic Forson [a,*], Aboagye Menyeh [b], David Dotse Wemegah [b]

[a] Department of Physics, School of Physical and Mathematical Sciences, College of Basic and Applied Sciences, University of Ghana, Ghana
[b] Geophysics Section, Department of Physics, Kwame Nkrumah University of Science and Technology, Ghana

ARTICLE INFO

Keywords:
Geophysical data
Remote sensing data
Mineralization
Center for Exploration Targeting (CET) grid analysis
Crosta PCA technique

ABSTRACT

Geophysical and remote sensing datasets were employed to delineate potential zones of gold mineralization within the southern Kibi-Winneba belt of Ghana. The study area, which is characterized by the Birimian metavolcanic and metasedimentary rocks with prevalence of intrusive granitoids hosts several scientifically unguided operational activities by artisanal miners locally referred to as Galamsey. In this study, various enhancement techniques were employed on geophysical datasets encompassing magnetic, gravity and radiometric to delineate various lithological units, which corroborated with the Birimian formation and its related granitoid intrusives within the study area. The Center for Exploration Targeting grid analysis and Line Module Algorithm techniques were employed respectively on the magnetic and Sentinel 2A datasets to delineate various structural lineaments within the study area. Approximately 72% and 67% structural lineaments delineated respectively from the magnetic and Sentinel 2A datasets trended in the NE-SW and N-S direction, which control gold mineralization within the Birimian system. The prinicpal component analysis based on the Crosta technique was employed on the Sentinel 2A bands to highlight alteration zones within the study area. A potential map of gold mineralization zones within the study area was generated by integrating exploration layers comprising magnetic, gravity, structural density, radiometric and alteration zones delineated by Crosta technique. This mineral potential map categorized the belt into low, moderately low, moderately high and highly prospective regions with area coverage of 600.4 km^2, 681.27 km^2, 635.95 km^2 and 295.20 km^2 respectively. The mineralization potential map obtained was validated with available gold geochemical data and locations of artisanal mining operations (Galamsey), which corroborated with the highly potential mineralization zones of gold deposits delineated within the study area.

1. Introduction

The southern Kibi-Winneba belt, which constitutes the southern half of the Kibi-Winneba volcanic belt, is one of the main northeast-southwest (NE-SW) trending gold belts in Ghana, whose mineralization style characterizes mesothermal quartz-vein deposits with disseminated sulphides encompassing pyrite and arsenopyrite as well as carbonate and sericite alterations (Eisenlohr and Hirdes, 1992; Klemd et al., 2002; Griffis et al., 2002). Although there is no discovery of commercial deposits of gold mineralization in the southern Kibi-Winneba belt, this gold belt shares geological resemblance with the Ashanti belt, owing to the overall synclinal structure characterising it (Eisenlohr, 1989; Dove, 1991; Eisenlohr and Hirdes, 1992). In view of this, Griffis et al. (2002) called for the need to employ efficient and systematic exploration techniques to ascertain the gold prospects within this part of the belt after observing a prominent north-east trending fracture zone as well as getting good results from geochemical analysis of soils in Gomoa Oguakrom, Gomoa Ajumako and Mumford, which are good indicators of gold occurrence in the area. Prevalent in this volcanic belt are several small scale and artisanal mining activities, whose operations are unguided by comprehensive geoscientific techniques to corroborate variously evident gold mineralization patterns. The actors in these artisanal mining operations, locally referred to as "Galamsey" in recent years have been under siege and their operations have been

* Corresponding author.
E-mail address: ericdforson@gmail.com (E.D. Forson).

https://doi.org/10.1016/j.oregeorev.2021.104271
Received 30 January 2021; Received in revised form 27 May 2021; Accepted 31 May 2021
Available online 23 June 2021
0169-1368/© 2021 Elsevier B.V. All rights reserved.

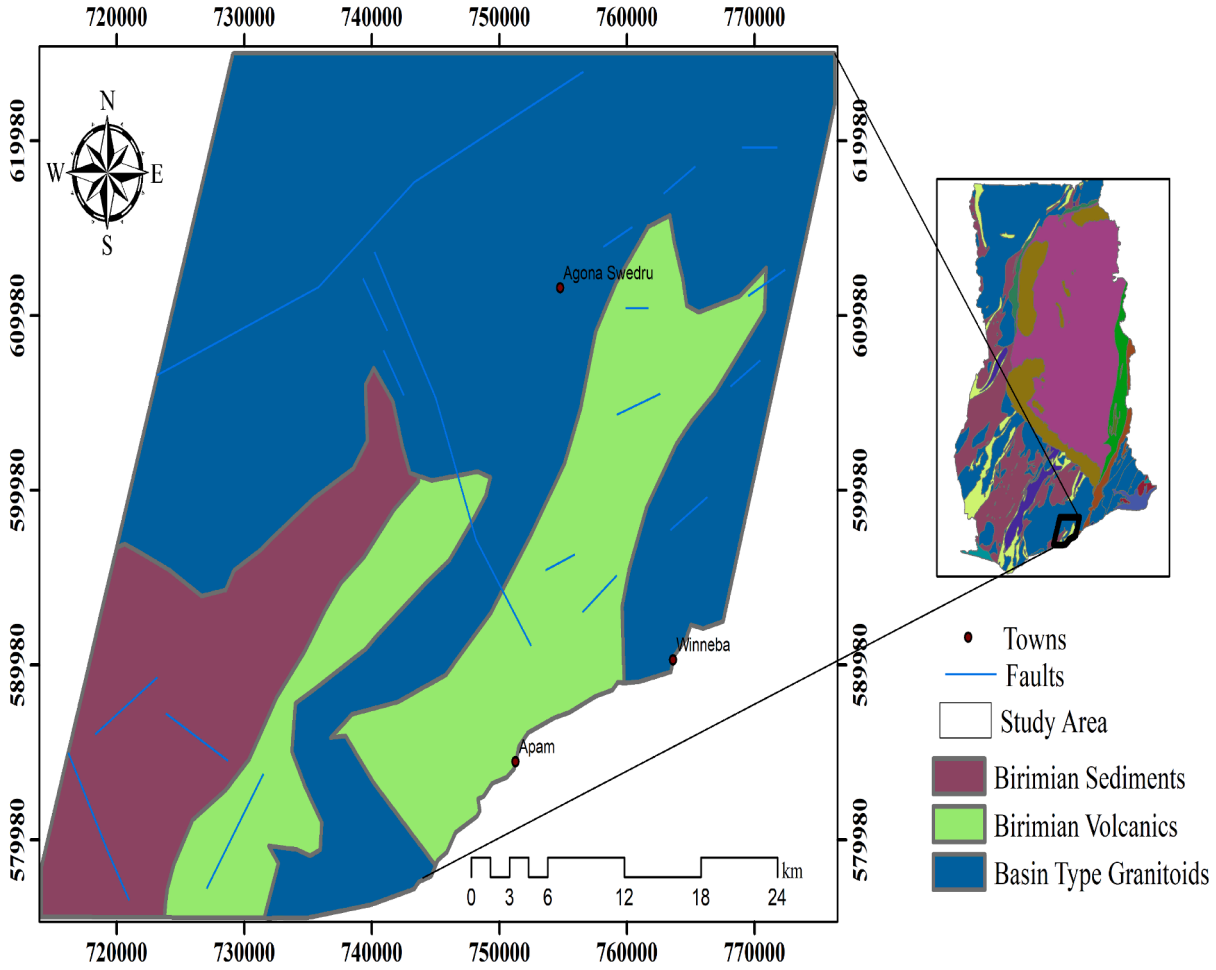

Fig. 1. Modified geological map of the southern Kibi-Winneba belt (Leube et al., 1990).

subsequently suspended by the Ghana Government owing to the enormous threat these unguided mining operations pose to water bodies, crop plantations and the environment as a whole (Hilson et al., 2007; Kessey and Arko, 2013; Boateng et al., 2014; Ontoyin and Agyemang, 2014; Boadi et al., 2016).

In spite of the geological resemblance of this belt with the Ashanti and Bui Belts, which generally points to it as a haven of considerable mineralization of gold, it remains an under-explored virgin area. This is exhibited in the lack of the application of various geophysical and remote sensing techniques in unravelling the prospectivity of the study area, though these techniques have played significant roles in mineral exploration and discovery of gold mineralized zones in many geological terranes around the world and with the dangers posed by these illegal mining operations, delineating prospectively viable zones of mineralization would be essential in fostering investor interest in mining operations within the area, which would be properly regulated against the ills associated with the illegal operations. (Jorgensen et al., 2002; Nykänen and Salmirinne, 2007; Shah et al., 2013; Pour and Ali, 2014; Wemegah et al., 2015; Brempong et al., 2019; Beiranvand Pour et al., 2019b; Zoheir et al., 2019; Bolouki et al., 2020; Traore et al., 2020; Wambo et al., 2020). Based on this premise, evidence of the employability of geophysical and remote sensing techniques to assist in the full realization of the gold mineralization potential within the southern part of the Kibi-Winneba belt is rare in the literature. In order to delineate the geological features associated with target zones of gold mineralization for further exploration work, geophysical and remote sensing techniques would be employed, due to their efficacy to delineate lithological unit, structural lineaments and hydrothermal alteration zones within an area (Dransfield et al., 1994; Schetselaar et al., 2000; Silva et al., 2003; Ramadass et al., 2013; Dufrechou et al., 2015; Pour and Hashim, 2015; Wemegah et al., 2015; Ramezanali et al., 2017; Beiranvand Pour et al., 2018; Beiranvand Pour et al., 2019a; Brempong et al., 2019; Pour et al., 2019; Pour et al., 2019; Sheikhrahimi et al., 2019; Zoheir et al., 2019; Pour et al., 2021b; Pour et al., 2021a). This present study, employs geophysical and remote sensing datasets encompassing magnetic, gravity, radiometric and Sentinel 2A MSI to delineate lithological units, structural lineaments and alterations zones, which would be integrated to generate a potential map of gold mineralization within the southern Kibi-Winneba belt. These datasets are of peculiar geological significance. For the radiometric method, differences in the distribution of various radioelements within the study area were vital in also delineating various units of lithologies. This is because, the three most important elemental concentration channels in radiometric data comprises thorium (eTh), potassium (K) and uranium (eU), and hence the three radioelements when integrated would play a primal role in geological or geochemical interpretation (McKinley et al., 2014; Ramadass et al., 2015). Gravity plays a primal role in making interpretations of meaningful geological inference. In a geologic environment, various lithological units differ in densities and hence anomalies observed from employing gravity data in geophysical studies also play a vital role in delineating various lithologies as well as geological structures within an area surveyed (Dentith and Mudge, 2014; Fairhead et al., 2017; Pinet et al., 2019; Thomas et al., 2019). In view of this, contrasts in density associated with gravity data in a particular area of study were also beneficial in outlining structurally-controlled mineralizations. It also noteworthy that, the primary aim upon which magnetic data are

employed in geophysical studies is to delineate various lithological and structural features within an area surveyed (Amenyoh et al., 2009; Malehmir et al., 2017; Walter et al., 2020; Liang et al., 2021). Hence the magnetic responses observed from aeromagnetic maps characterizes the concentration of magnetic minerals associated with various lithologies (rock formations). These maps were also vital in delineating structural lineaments, which are significant pathfinders for gold mineralization within the southern Kibi-Winneba belt. Furthermore, remote sensing methods generally rely on spectral data acquired by remote sensing scanners as energy reflected from or emitted by the surface of the Earth. As a result, datasets obtained from remote sensing surveys such as Sentinel-2 have over the years proven essential in mapping various alteration zones as well as structural mapping. In view of these characteristic relevance of the remote sensing method, it delineated various iron and hydroxyl alteration zones in the study area (Magiera, 2018; Salehi et al., 2019; Sekandari et al., 2020a; Frutuoso et al., 2021). It also complemented the magnetic method in delineating various lineaments, which are characteristic of gold mineralization within the area under study. Also, available geochemical datasets as well as various locations of artisanal mining (Galamsey) occurrences would be employed to evaluate how the potential targets zones of gold mineralization, obtained from the integration of the geophysical and remote sensing datasets correlate.

2. Geological setting

The area under investigation, which lies within eight administrative districts and geologically falls within the southern Kibi-Winneba volcanic belt in the Central Region of Ghana, contains part of the Birimian formation and covers a total landmass of 2226.01km^2 (Senayah et al., 2010). This belt is one of the six main greenstone volcanic belts associated with the Palaeoproterozoic Birimian Supergroup found in Ghana. All of these belts, with the exception of one (Wa-Lawra greenstone belt, which trends northwest) trend in the north-eastern (NE) direction and lie side by side against each other, featuring the occurrence of gold mineralization (Dzigbodi-Adjimah, 2004). The Kibi-Winneba volcanic belt however, stretches from Winneba along the coast in the Central Region, strikes north–northeastern (NNE) for about 100km towards Kibi and beyond in the Eastern Region. It features an overall synclinal-structure resemblance with the Ashanti and the Bui belts and is divided into two parts (northern and southern part) by the Cape Coast granitoid (Eisenlohr, 1989; Eisenlohr and Hirdes, 1992). The northern part falls within the Kibi town and its environs in the Eastern Region and are prevalently characterized by Tarkwaian sediments surrounding Birimian volcanic rocks. The southern part, however falls within Winneba town and its environs in the Central Region and predominantly features basin-type granitoids and is associated with Birimian volcanic and sedimentary rocks (Eisenlohr and Hirdes, 1992; Klemd et al., 2002). Fig. 1, which represents geological formations within the southern Kibi-Winneba belt particularly, have been deformed immensely and metamorphosed to facies of upper greenschist-lower amphibolite coupled with evidence of broad folded-isocline and various shear systems throughout the belt. In this regard, this part of the belt features broad emplacements of granitoids, which are interpreted as steep contact intrusions, whose placement are fairly confined. The southern part of the study area, features well exposed unweathered amphibolites and quartz-mica schists comprising varying proportion of quartz, muscovite as well as oxide and sulphide minerals (hematite, pyrite and arsenopyrite) (Klemd et al., 2002). It also features the Winneba-type granitoids, known in recent literature as the belt type intrusive rocks (Dzigbodi-Adjimah, 2004). The concentration of broad pegmatites featuring aplites and quartz veins which are found in several areas within the belt are generally more close to the contacts of large extent associated with the basin-type granitoids. Mafic intrusives within this part of the belt seem to comprise predominantly north–southern (N-S) trending sills and dikes subjected to early stage metamorphism and a few dolerite dikes, which have not been metamorphosed (Griffis et al., 2002). Other regions within the study area are characterized by Birimian volcanic dominant domain mainly comprising amphibolite, schist, phyllite and greywacke whose origin could be traced with partial contact metamorphism occurrence (Klemd et al., 2002). It is characterized by basic intrusives such as epidiorite, hornblendite as well as few minor intrusives like quartz, pegmatite and aplite veins. Gold mineralization in other areas within this belt is mostly within a foliated granodiorite associated with shearing, silicification and quartz stingers (Newmont, 2006; Adjovu, 2007). The southern Kibi-Winneba belt however, is geologically synonymous to the renowned Ashanti belt and has a prospective potential for gold deposits (Klemd et al., 2002; Dzigbodi-Adjimah, 2004).

3. Method

3.1. Datasets

In this research, the geophysical and remote sensing datasets encompassing magnetic, gravity, radiometric and Sentinel 2A MSI obtained from credibly established data sources were the main spatial datasets employed. The aeromagnetic and aeroradiometric datasets were acquired by the Geological Survey of Finland (GKT) in collaboration with Ghana Geological Survey Authority (GGSA) in 1998 with terrain clearance and profile line spacing of 70m and 400m respectively. Gravity data employed is that of the EGM2008 Bouguer anomaly, with gravity sample spacing of 100m and was obtained from the GFZ German Research Centre for Geosciences (www.gfz-potsdam.de). Remote sensing datasets encompassing Sentinel 2A MSI was also obtained from the United States Geological Survey Earth Resources Observation and Science Center (www.usgs.gov/centers/eros) on October 2nd, 2018. Geochemical datasets of gold within the study area were also obtained from GP Minerals Company Limited and Newmont Ghana Gold Limited.

3.2. Processing of geophysical and remote sensing datasets

3.2.1. Processing and enhancements of geophysical datasets

Each of these potential field (gravity and magnetic) datasets comprising bouguer anomaly and total magnetic intensity (TMI) were imported into the Geosoft Oasis Montaj software. This was succeeded by the removal of Geomagnetic Reference Field (IGRF) from the magnetic data to attain residual magnetic intensity (RMI). Corrections for topographic effects were made to the bouguer anomaly map to obtain a complete bouguer anomaly map (CBA). The butterworth filter was employed on each of the RMI and CBA to enhance the CBA and RMI. For the magnetics, the enhanced RMI was reduced to pole using the reduction to pole (RTP) and analytic signal (AS) filter to place the anomalies precisely on top of the source producing those anomalies. The first vertical (1VD) and tilt derivatives (TDR) filters were employed on the RTP to delineate linear structures within the study area. Residual gravity map was generated from the enhanced complete bouguer anomaly (CBA) based on Gaussian Regional/Residual Filtering in Geosoft Oasis Montaj Software (Blakely and Simpson, 1986; Blakely, 1995).

The Centre for Exploration Targeting (CET) grid analysis technique in Geosoft was employed on the RTP magnetic grid to emphasize discontinuous zones within the study area. These prevalent regions of magnetic discontinuity are depicted by several skeletons of various structures upon the application of texture enhancements. This results in the generation of an output grid comprising several discontinuously skeletal line segments, depicting various structural features with varying offsets and orientations (Kovesi, 1997; Xiao et al., 2005; Holden et al., 2011).

Aeroradiometric datasets employed in this research comprised mainly three channels of potassium (K), equivalent thorium (eTh) and equivalent uranium (eU) concentration. Processing of this dataset comprised the gridding of individual elemental channels, channel ratios as well as the generation of a ternary map Geosoft Oasis Montaj

Table 1
Characteristics of Sentinel-2 Metadata.

Sentinel-2 Bands	Central Wavelength (μm)	Resolution
Band 1 - Coastal aerosol	0.443	60
Band 2 - Blue	0.490	10
Band 3 - Green	0.560	10
Band 4 - Red	0.665	10
Band 5 - Vegetation Red Edge	0.705	20
Band 6 - Vegetation Red Edge	0.740	20
Band 7 - Vegetation Red Edge	0.783	20
Band 8 - NIR	0.842	10
Band 8A - Vegetation Red Edge	0.865	20
Band 9 - Water Vapour	0.945	60
Band 10 - SWIR - Cirrus	1.375	60
Band 11 - SWIR	1.610	20
Band 12 - SWIR	2.190	20

Table 2
PCA results of selected bands 2, 8, 11 and 12 of Sentinel-2A for Hydroxyl minerals.

Bands/PC	PC1	PC2	PC3	PC4
Band 2	- 0.08127	−0.05145	0.95861	0.26800
Band 8	0.16147	0.95798	0.09807	−0.21585
Band 11	0.74675	0.03812	−0.23490	0.62108
Band 12	−0.64007	−0.27961	0.12759	−0.70417
Eigenvalue	112365.56369	80444.43978	5815.68815	2057.81661
Percentage of Eigenvalue	55.9914	40.0852	2.8979	1.0254
Accumulative of Eigenvalues	55.9914	96.0767	98.9746	100.0000

Table 3
PCA results of selected bands 2, 4, 8 and 11 of Sentinel-2A for Iron oxide minerals.

Bands/PC	PC1	PC2	PC3	PC4
Band 2	0.02045	−0.14693	0.70030	0.69826
Band 4	0.01646	0.36187	0.61870	−0.69713
Band 8	0.82215	−0.53103	0.18192	−0.09478
Band 11	0.56867	0.75198	−0.30610	0.13210
Eigenvalue	87787.13095	61125.86347	907.83177	475.31489
Percentage of Eigenvalue	56.7515	37.2616	5.7458	0.2411
Accumulative of Eigenvalues	56.7515	94.0131	99.7589	100.0000

Table 4
Edge detection and line extraction thresholds employed in the study.

Threshold Names	Description	Threshold values
Filter radius (RADI)	For the detection of edges	12
Edge gradient (GTHR)	For the detection of edges	50
Curve length (LTHR)	minimum length of a curve taken as lineament	25
Line fitting error (FTHR)	Allowed tolerance in curve fitting to form a polyline	3
Angular difference (ATHR)	Maximum angle between two linked polylines	20
Linking distance (DTHR)	Maximum distance between two linked polylines	1

Software. The minimum curvature algorithm was employed on the radiometric dataset to generate individual grids for K, eTh and eU. The gridmath algorithm was subsequently used to generate channel ratio maps which encompassed eU/K and K/eTh. These ratio maps were generated with the intent of highlighting regions of high uranium concentration as well as potassium metasomatism which are associated with possible gold occurrences (Dickson and Scott, 1997). A ternary map which is a model comprising the integration of all the three radiometric channels (K, eTh and eU) where K, eTh and eU are assigned red, green and blue colours respectively. Final radiometric grids exported to geotiff file extension for further analysis, interpretation and final map making in ArcGIS comprised mainly K, K/eTh, eU/K and Ternary map.

3.2.2. Preprocessing, processing and enhancement of remote sensing imageries

The main remote sensing data employed in this research was the Sentinel 2A MSI and was acquired at L1C (radiance to the sensor) level with no cloud cover and hence preprocessing was devoid of radiometric correction on the imageries. Atmospheric correction was however carried out on the data to remove atmospheric effects on the reflectance values associated with the images. The metadata characteristics of the Sentinel-2A MSI is shown in the Table 1. The principal component analysis and the Crosta Technique were employed on the remote sensing imagery to enhance and delineate possible hydrothermal alteration zones (Goetz and Roman, 1981; Sabins, 1999; Dehnavi et al., 2010; Beiranvand Pour et al., 2019b). The principal component analysis (PCA) was employed on the selected bands (2, 8, 11 and 12 for hydroxyl minerals and 2, 4, 8 and 11 for iron bearing minerals) of the remote sensing data to help determine the eigenvector loadings of bands (shown in Tables 2 and 3) capable of delineating various distinctive mineralized zones having hydroxyl and iron minerals being prevalent by using the Erdas Imagine software. This selective method of bands for PCA, responsible for highlighting iron and hydroxyl alterations is referred to as Crosta technique (Ranjbar et al., 2004; Liu et al., 2011; Beiranvand Pour et al., 2018; Moradpour et al., 2020; Beygi et al., 2020; Sekandari et al., 2020b). The principal component analysis (PCA) is an effective and a precise technique for delineating zones of mineral alteration from a multispectral dataset. The PCA based on the Crosta technique was employed to delineate hydroxyl bearing minerals by combining bands 2, 8, 11 and 12 of Sentinel 2A imagery, whose PCA results are shown in Table 2. This table contains results obtained for the eigenvectors, eigenvalues, percentage and accumulative eigenvalues of the four principal components generated for the selected hydroxyl bands. Iron bearing minerals were also delineated by combining bands 2, 4, 8 and 11 of Sentinel 2A imagery. Table 3 contains the PCA results of the selected iron oxide bands encompassing 2, 4, 8 and 11. The PCI Geomatica software was also employed on remote sensing imagery to extract lineaments within the study area. The lineament extraction first comprised the combination of the spectral bands. The Input Params1 column under the LINE MODULE ALGORITHM within the PCI Geomatica software was then used to automatically extract the linear features. The LINE MODULE ALGORITHM menu operates on two main stages of processing (edge detection and line extraction). The first processing stage (edge detection algorithm) enhances the pixels at the edges of the combined spectral bands (Kocal et al., 2004; Abdullah et al., 2010). The line extraction stage (second processing stage) was carried out to remove falsified responses of edges and to connect the gaps between the edges, so as to turn edges that are isolated into linear features. In the PCI Geomatica software, six different thresholds were set to characterize the edge detection and line extraction processes. These thresholds as shown in the software encompassed RADI (filter radius), GTHR (edge gradient), LTHR (curve length), FTHR (line fitting error), ATHR (angular difference) and DTHR (linking distance). Edge detection is effectively carried out by the RADI and GTHR thresholds whereas the line extraction is also carried out by the other four thresholds (Thannoun, 2013; Ahmed, 2014). Threshold values employed to automatically extract the lineament in the PCI Geomatica software is shown Table 4.

3.3. Generation of mineral potential map

In this study, the five (5) evidential layers obtained from the aero-

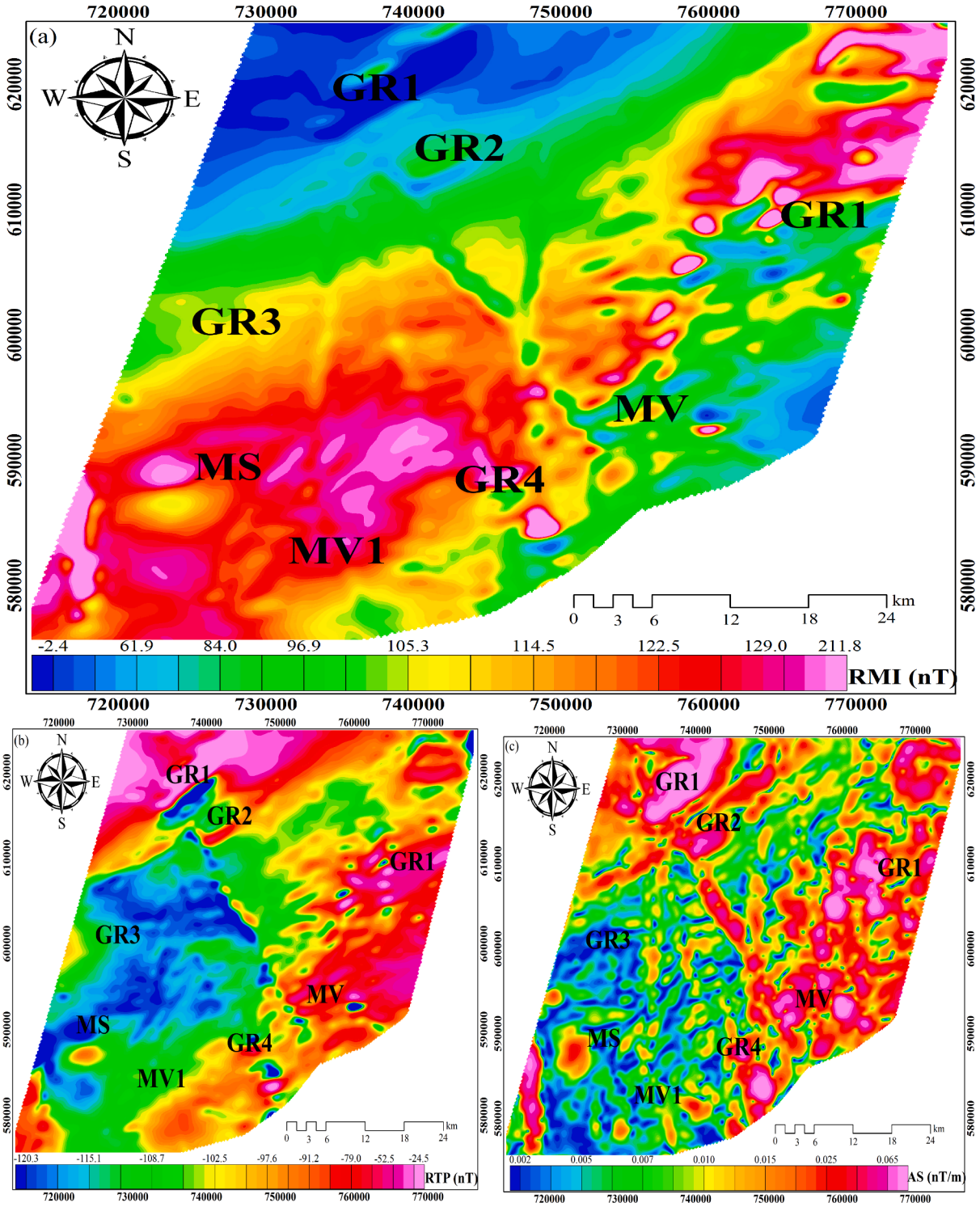

Fig. 2. (a) RMI of the southern Kibi-Winneba belt; (b) RTP map of the southern Kibi-Winneba belt (c) Analytic signal map of the southern Kibi-Winneba belt.

magnetic, satellite gravity, aeroradiometric and Sentinel-2 datasets were integrated to produce a mineral potential map of gold within the study area. Each of these evidential layers were classified into four and were subsequently normalized based on Eq. 1 to make each evidential layer be characterized by values ranging from 0 to 1.

$$X_{normalized} = \frac{X - X_{minimum}}{X_{maximum} - X_{minimum}} \quad (1)$$

X, $X_{normalized}$, $X_{minimum}$ and $X_{maximum}$ denote the evidential layer, normalized evidential layer, minimum value of the evidential layer and maximum value of the evidential layer respectively. Each of these evidential layers were then multiplied by their respectively assigned weights owing to their relative importance to gold mineralization within the study area and were subsequently integrated based on the weighted overlay method shown in Eq. 2.

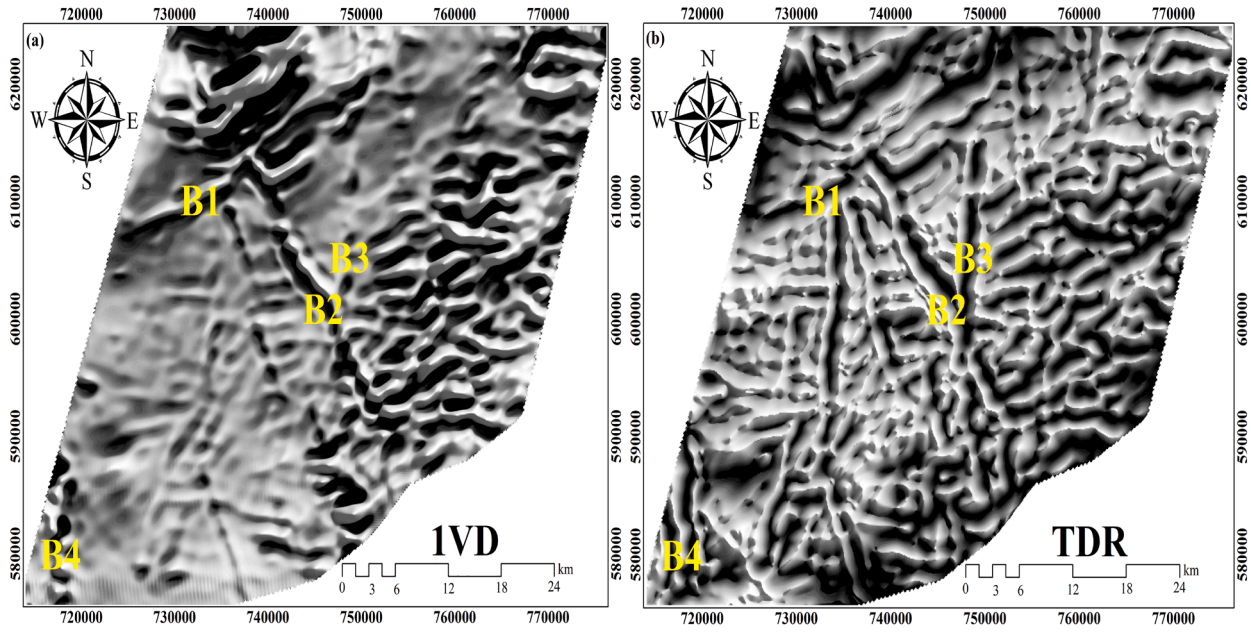

Fig. 3. (a) First vertical (1VD) map of the southern Kibi-Winneba belt; (b) Tilt derivative (TDR) map of the southern Kibi-Winneba belt.

$$S = \frac{\sum_{i}^{n} S_{ij} W_i}{\sum_{i}^{n} W_i} \quad (2)$$

Where S denotes the weighted value assigned to each evidential layer, S_{ij} denotes the score of the j-class of the ith evidential layer, W_i is the weight of the ith evidential layer entered and j depicts the class which ought to be weighted and scored in the evidential layers under consideration. The mineral potential map obtained was then subsequently normalized based on Eq. 1 (Yousefifar et al., 2011; Abuzied et al., 2016).

4. Results

4.1. Aeromagnetic

4.1.1. Residual Magnetic Intensity (RMI), Reduction to Magnetic Pole (RTP) and Analytic Signal (AS) Maps

The RMI shown in Fig. 2(a) depict asymmetric magnetic responses relative to the various lithological units within the southern Kibi-Winneba belt. This asymmetric effect associated with the RMI made the observed magnetic anomalies not reflective of the causative bodies (lithological units). For instance, regions within the study area characterized by metavolcanic **(MV)** rocks which are rich in iron bearing minerals owing to their maficity were observed to correspond to low to moderate magnetic intensity (-2.4 nT to 114.5 nT) instead of high magnetic intensity (114.5 nT to 211.8 nT). Also, the metasediments **(MS)** which should be associated with low to moderate magnetic signals (-2.4nT to 114.5nT) are observed to correspond to high magnetic intensity response (114.5 nT to 211.8 nT) on the RMI map (in Fig. 2(a)) (Klemd et al., 2002). To help solve this problem of asymmetric effect associated the RMI responses with respect to causative magnetic bodies, the reduction to pole (RTP) and analytical signal (AS) maps shown in Figs. 2(a) and (b) were generated to place the observed magnetic anomalies exactly on top of the source bodies creating those anomalies. Regions characterized by metavolcanic rocks **(MV)**, whose maficity owing to predominance of iron and sulphide minerals (such as pyrrhotite, hematite, arsenopyrite, pyrite and chalcopyrite) which are associated with quartz-vein deposits within the study area show high magnetic anomalies on the RTP (as -97.6nT to -24.5nT) and AS (as 0.015nTm^{-1} to 0.065nTm^{-1}) maps (Fig. 2(b) and 2(c)) in contrast with the low magnetic anomalies observed on the RMI (Fig. 2(a)) (Klemd et al., 2002; Nyarko et al., 2012). Metasedimentary **(MS)** regions within the study which depicted high magnetic intensity on the RMI map showed low to moderate magnetic intensity (-120.3 nT to -97.6 nT on RTP map and 0.002 nTm^{-1} to 0.015 nTm on the AS map) after it had been transformed to magnetic pole shown in Fig. 2(b). The study area has a significant history of metamorphism with the intrusion of granitoids within the Birimian Formation (Griffis et al., 2002; Klemd et al., 2002). In this regard, regions within the study area, which are lithologically characterized by the prevalence of hornblende and biotite granodiorite rocks correspond to the high magnetic signature (**GR1**) on the RTP and AS maps (Figs. 2(a) and (b)) (Anum et al., 2015). This highly magnetic signature (**GR1**) corresponds also to possible occurrence of strong disseminated sulphides within granodiorites with pyrite prevalent with magnetite inclusions (Tetteh and Effisah-Otoo, 2017). A highly magnetic response (**GR2**) observed within the northwestern part of the study area also corresponds with granitoids predominated by iron minerals as well as amphibolites, which is ferromagnesian and widespread within the study area (Klemd et al., 2002; Airo, 2015; Anum et al., 2015). These amphibolites (ferromagnesian), which are widespread within the study area have pyrite occurrences within their alteration halos in contact with magnetite (Tetteh and Effisah-Otoo, 2017).

Also, bulk magnetic properties of host rocks as well as intrusions are primarily controlled by iron oxides and silicates and hence highly magnetic regions within the intrusive granitoids (**GR1** and **GR2**) depict an indication of iron-oxide and silicate rich minerals associated with quartz-vein deposits and disseminated sulphide formations within the study area (Clark, 1999). Low magnetic regions within the basin type granitoids **(GR3)** correspond to the predominant existence of felsic minerals which characterize granitic lithological units. The analytic signal was also vital in delineating edges of magnetic source bodies as well as structural features within the study area. Structural features marked **B1**, **B2**, **B3** and **B4** trending respectively northeastern (**NE**), northwestern (**NW**), north–south (**N-S**) and north–south (**N-S**) were also highlighted on the analytic signal map. These marked structural features delineated on the analytic signal map were also delineated on the first vertical derivative (**1VD**), tilt derivative (**TDR**) as well as the lineament map delineated by using the Centre for Exploration Targeting (CET) analysis map.

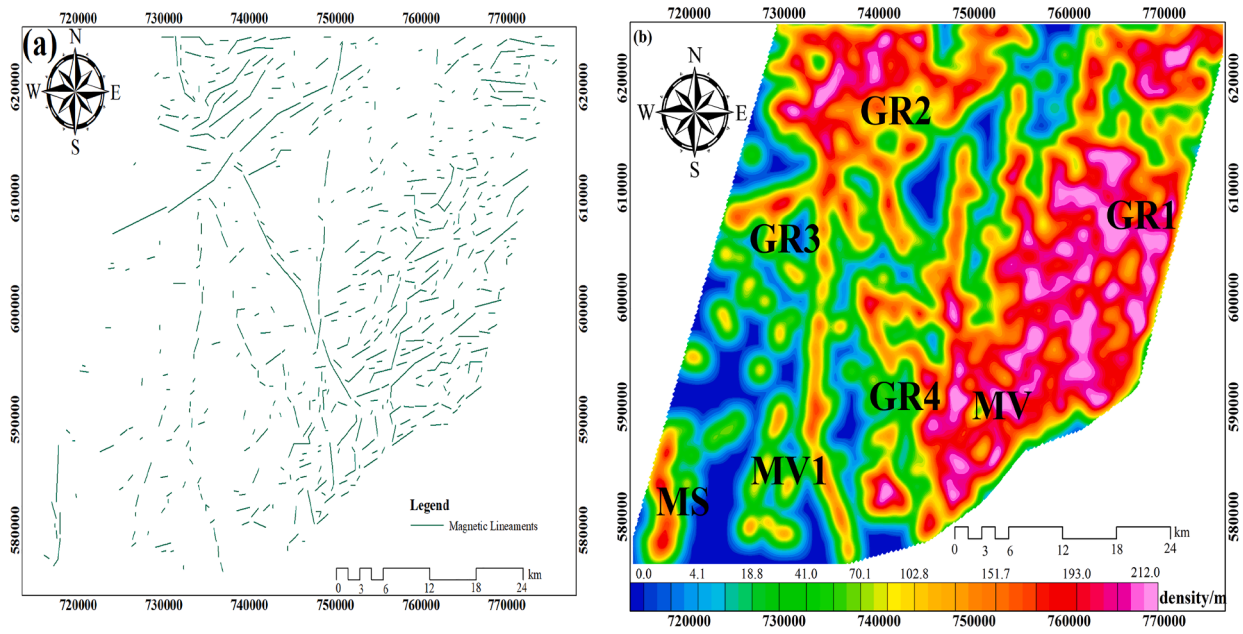

Fig. 4. (a) CET lineaments map of southern Kibi-Winneba belt (b) Structural complexity (density) map of southern Kibi-Winneba belt from the magnetic data.

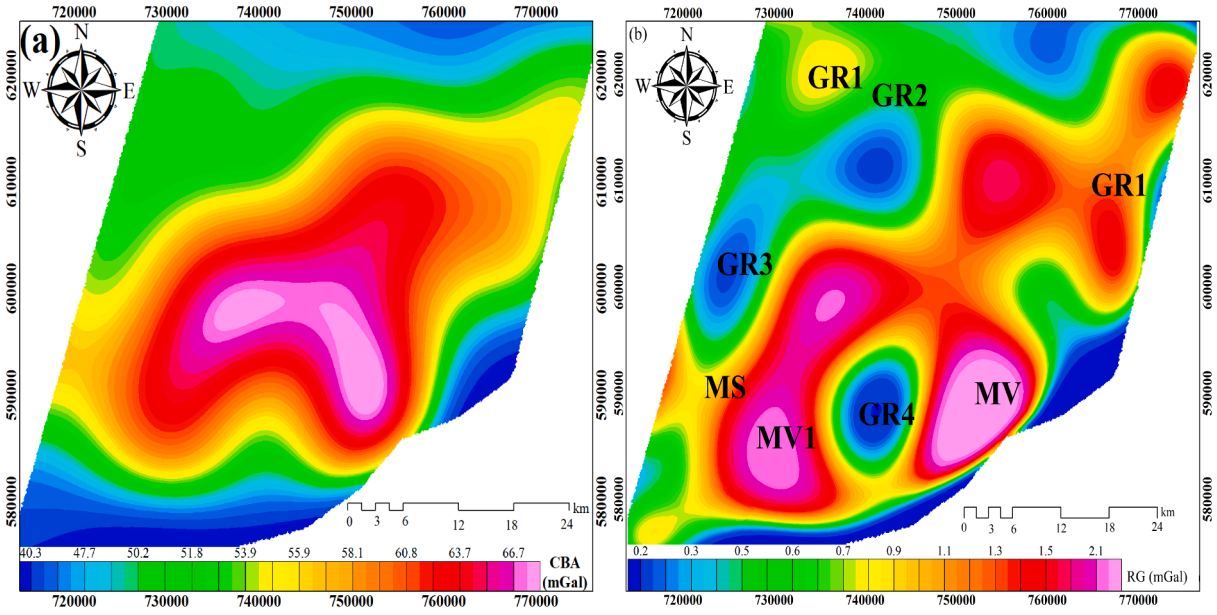

Fig. 5. (a) Complete bouguer anomaly map of southern Kibi-Winneba belt (b) Residual gravity map of the southern Kibi-Winneba belt.

4.1.2. First Vertical Derivative (1VD) and Tilt Derivative (TDR) Magnetic Map

The maps shown in Fig. 3 represent the first vertical derivative (3(a)) and the tilt derivative (3(b)) maps of the study area. The 1VD was vital in suppressing broad and more regional magnetic anomalies while enhancing the near surface anomalies associated with various structural features within the study area (Hinze et al., 2013). The TDR was also vital in detecting elusive geological boundaries of various delineated structures as well as highlighting considerable contrast in magnetic anomalies and to visualize various structural features, depicted as lineaments within the study area (Oruç and Selim, 2011). Notable among the delineated lineaments are **B1**, **B2**, **B3** and **B4** which have also been delineated on the 1VD (in Fig. 3) and analytic signal map (in Fig. 2(c)). Virtually all the linear features enhanced on the first vertical derivative map also correspond to the lineaments delineated by virtue of CET analysis on the RTP grid in Fig. 4(a).

4.1.3. Center for Exploration Targeting (CET) Analysis of Lineaments and Structural Density for Magnetic Data

CET grid analysis was employed on the RTP grid, several lineaments trends encompassing inferred major and minor faults within the southern Kibi-Winneba belt were delineated. The CET structural map shown in Fig. 4(a) also delineated the inferred structural features comprising **B1** (north-east trending structure), **B2** (north-west trending structure), **B3** (north–south trending structure) and **B4** (north–south trending structure) which have been delineated by on the analytic signal, first vertical derivative and tilt derivative magnetic maps shown in Figs. 2(c), 3(a) and 3(b) respectively. The structural density map obtained for the magnetic data in Fig. 4(b) is depicted by high, moderate and low regions of structural complexity and are denoted by red, green and blue

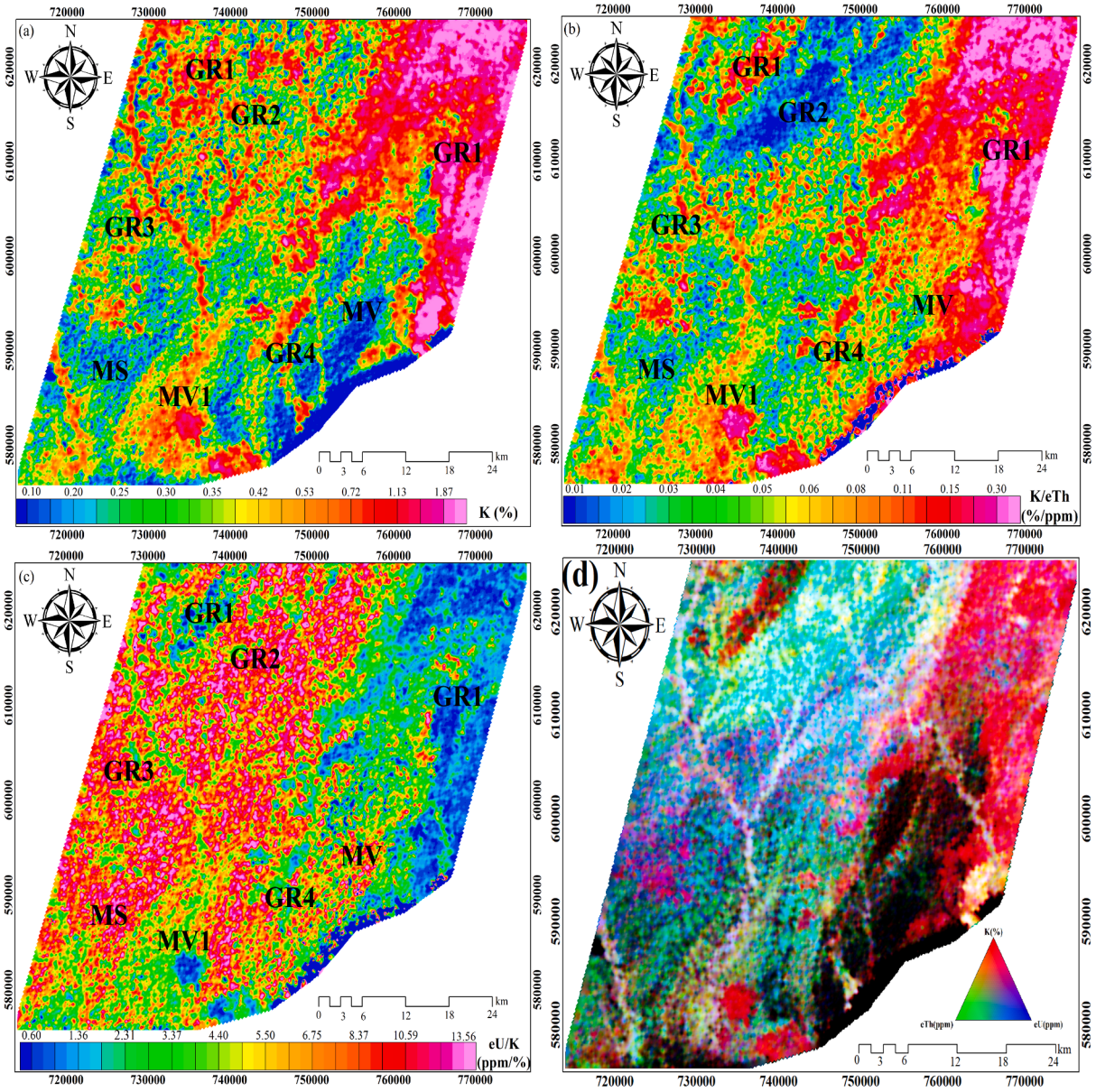

Fig. 6. (a) Potassium (K) concentration map of southern Kibi-Winneba belt (b) Potassium-Thorium (K/eTh) ratio map of the southern Kibi-Winneba belt (c) Uranium-Potassium (eU/K) ratio map of the southern Kibi-Winneba belt (d) Ternary radiometric map of the southern Kibi-Winneba belt.

respectively. It can be observed that, the region delineated as highly magnetic (in Figs. 2(b) and (c)), highly anomalous in gravity (in Fig. 5 (b)), highly anomalous in potassium (in Fig. 6(a)) as well as high region of hydroxyl and iron alteration (**GR1**) (in Fig. 7(d)) was also observed to be of high structural density. **GR2** and **MV** depicting possible alteration zones within the granitoids and metavolcanic formations were delineated as a highly dense lineament region. Considerable zones within the metasedimentary (**MS**) and metavolcanic (**MV1**) regions were observed to show moderate to high structural densities.

4.2. Complete bouguer anomaly and residual gravity results

Fig. 5(a) and Fig. 5(b) shows a gridded image of the complete bouguer anomaly (CBA) and the residual gravity maps respectively. The CBA, though has the capability to give some insight into the geometry and lithology of subsurface rocks, its observed anomalies were due to regional effects resulting from deep gravity anomalous sources. The residual gravity map (Fig. 5(b)) shows the distribution of various rock densities emanating from gravity signatures associated with local and shallow geological features within the study area (Blakely and Simpson, 1986; Blakely, 1995). In view of this, residual gravity responses emphasized most crustal geological and structural features owing to the removal of regional effects from geological features as shown in the complete bouguer anomaly map (Fig. 5(a)). These gravity anomalies observed from the residual gravity map (in Fig. 5(b)) make more geological sense to various near surface features than the gravity signatures observed on the complete bouguer anomaly map. These anomalous zones of gravity, distinctively outlined boundaries depicting contacts between different geological formations within the study area. In this regard, the residual gravity anomaly map delineated the Birimian metavolcanic formations (**MV** and **MV1** with high gravity anomaly response from 1.1 mGal to 2.1 mGal) within the area, whose maficity owing to possible enrichment of iron (Klemd et al., 2002) associated minerals made it more denser than all other delineated lithologies within the study area. The residual gravity map also delineated regions within the study characterized by metasediments (**MS**), whose gravity responses are low to moderate (0.2 mGal to 1.1 mGal). Regions within the basin type granitoids, observed to be highly magnetic on the

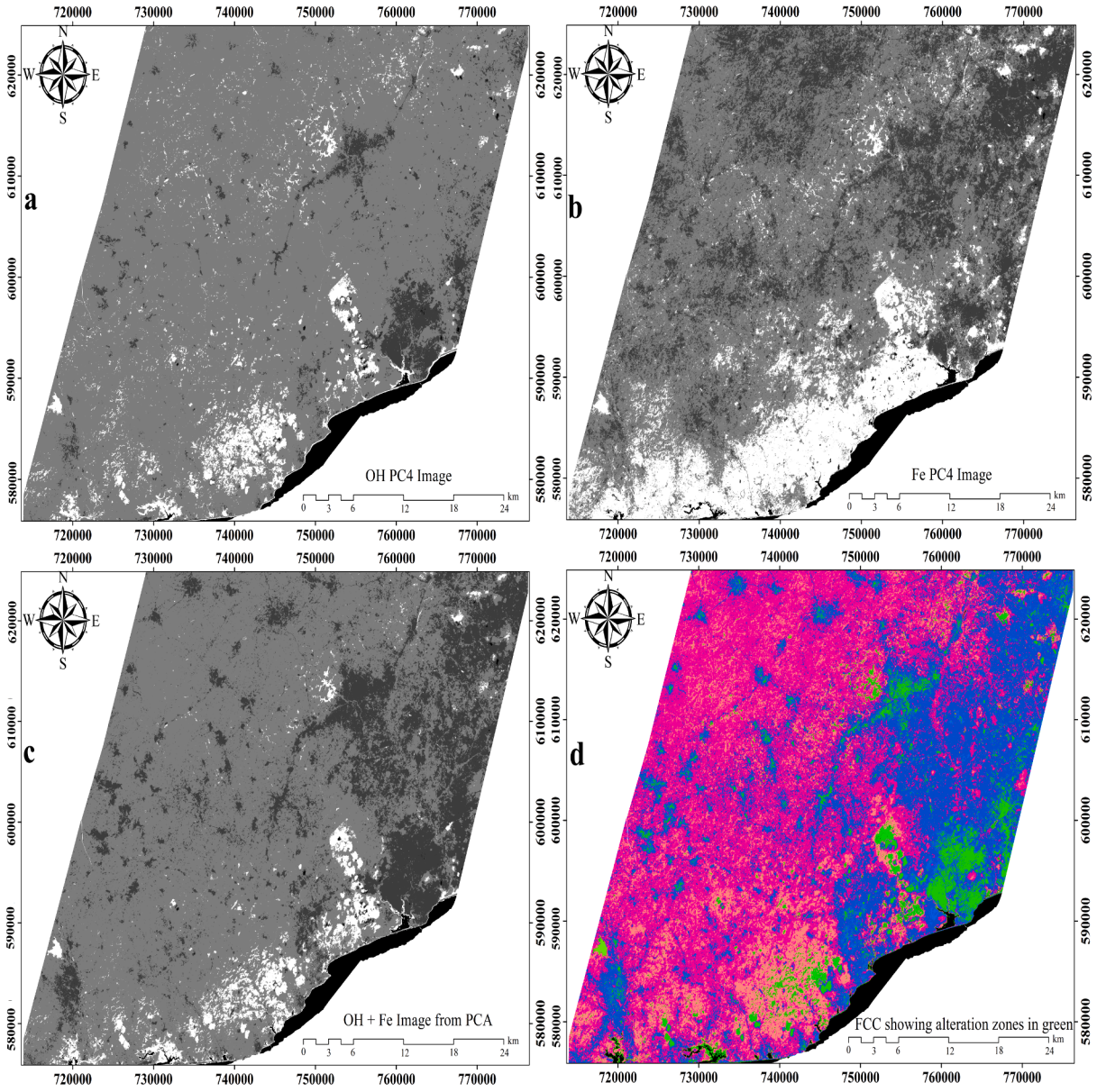

Fig. 7. Map of Crosta technique (a) OH image (b) Fe image (c) OH + Fe (d) Colour composite image of OH, Fe, OH + Fe in R, G, B respectively.

reduction to pole and analytic signal maps (**GR1**) and (**GR2**) were also observed to show high and moderate anomalies respectively on the residual gravity map. These moderate and high gravity signatures observed for **GR1** and **GR2** corresponds to possible accumulation of iron owing to amphibolites, biotite granodiorites, chalcopyrite and pyrite minerals within these intrusive granitoid formations since gravity shows positive anomalies within regions of magmatic intrusions (Kamguia et al., 2005; Adjovu, 2007; Anum et al., 2015). **GR3**, which depicted regions within the basin type granitoids showing low magnetic response on the RTP and AS maps owing to the possible accumulation of felsic-dominant granitic rocks was also observed to show low gravity signature. Another anomalously low, but nearly spherical gravity signature labelled as **GR4** was delineated to be sandwiched between delineated lithologies labelled **MV** and **MV1** on the residual gravity map (Fig. 5(b)). This nearly spherical anomalous body (**GR4**) depicts the belt type granitoids which intrudes the Birimian volcanic rocks in the study area (Dzigbodi-Adjimah, 2004).

4.3. Aeroradiometric results

In this research, radiometric channel ratio maps were generated to see how each radioelement compares with the other in a particularly lithological framework within the study area. A ternary map was also generated to display how the three radioelements (K, eU and eTh) are distributed relative to each other in the study area. The ternary map enables the qualitative categorization of the chemical signature as well as the discrimination of various units of lithologies based on the colouration inferred from within the image obtained for study area (Dentith and Mudge, 2014). In this study, the radiometric maps (Figs. 6(a), 6(b), 6(c) and 6(d)) played a primal role in delineating eminent lithological and alteration zones within the southern Kibi-Winneba belt. Results from these K, K/eTh, eU/K and Ternary radiometric signatures delineated **GR1** lithological unit, observed to be covering most regions of the eastern part. A portion of the northwestern part of the study area was observed to be highly potassic (as 0.08 %/ppm to 0.30 %/ppm on potassium-thorium ratio map in Fig. 6(b)) with low thorium concentration as well as moderate to high uranium within an intrusive granitoid formation. Uranium enrichment is an evidence of possible mineral

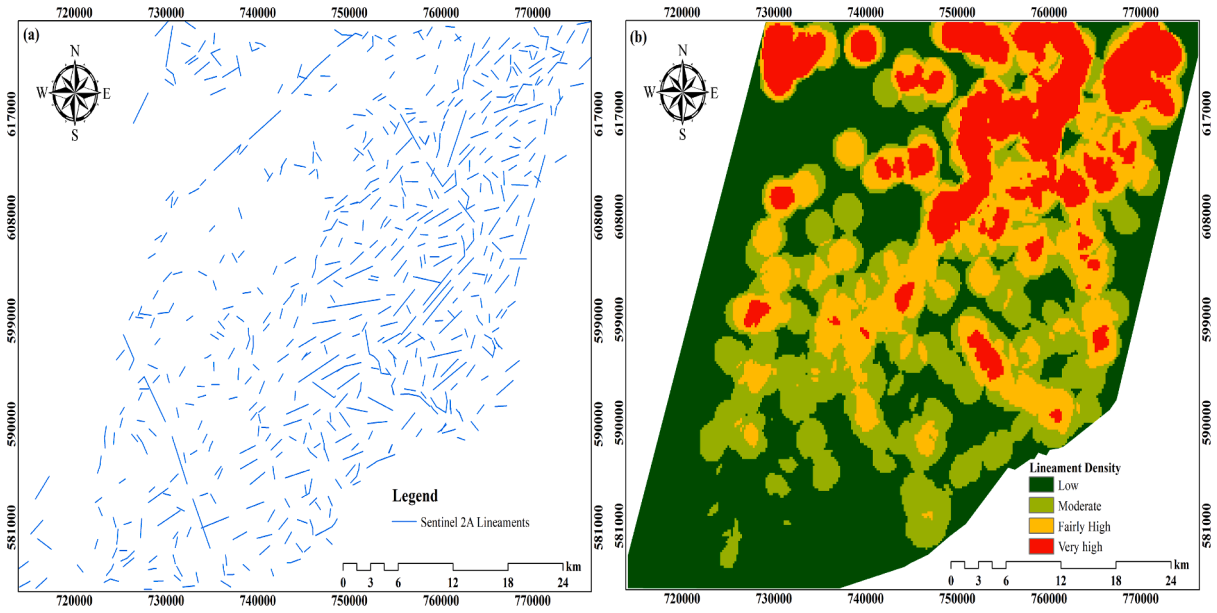

Fig. 8. (a) Extracted lineaments map of southern Kibi-Winneba belt from remote sensing data (b) Structural density map of southern Kibi-Winneba belt from the remote sensing data.

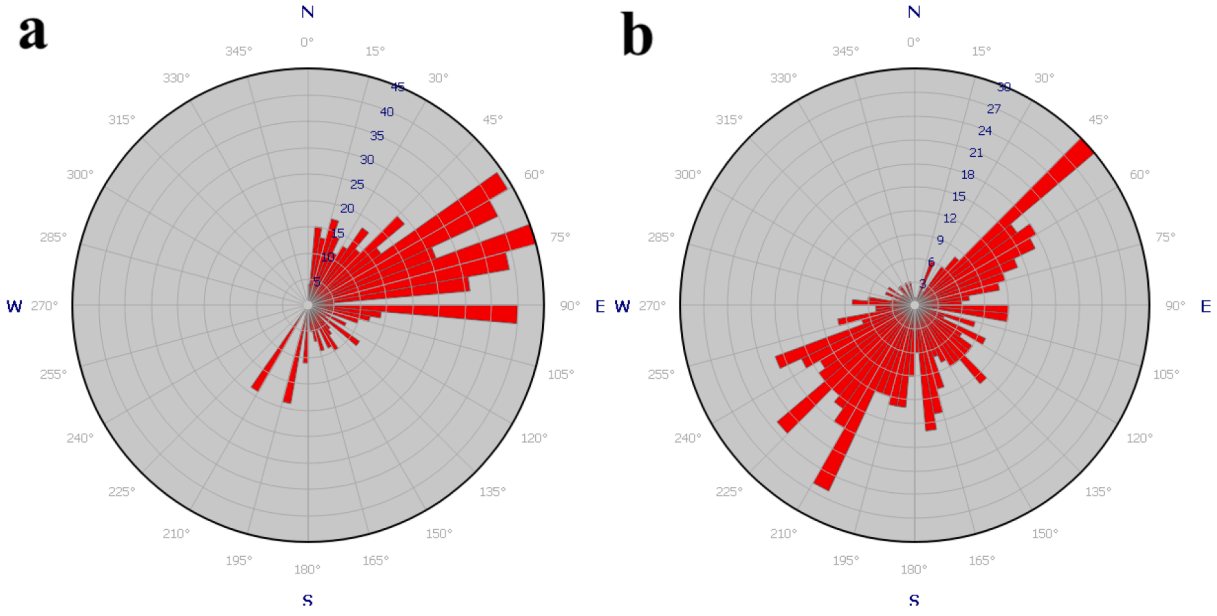

Fig. 9. (a) Trends of magnetic lineaments shown by the Rose diagram(b) Trends of Sentinel-2A lineaments shown by the Rose diagram.

enrichment. Potassium and thorium antagonism, owing to increased potassium concentration against the depletion thorium could also result in potassium metasomatism (Ostrovskiy, 1975; Sobolev et al., 2018). This gives an indication of possible potassic alteration occurrence with prevalence of granodiorite within the northeastern part of the study area (**GR1**) owing to its highly magnetic and gravity anomalies as well as highly potassic signatures observed (shown Fig. 6(a) as 0.53 %K to 1.87%K). **GR2** formation was also observed to be characterized by high thorium concentration as against moderate to high potassium concentration within the northwest part of the study area. The magnetically high anomaly, as well as moderate gravity signature observed within the area gives an indication of hydrothermal alteration with oxide minerals (commonly magnetite) with prevalence of hornblende associated minerals such as amphibolites (Klemd et al., 2002; Nyarko et al., 2012). The delineated **GR3** radiometric region, was observed to show moderate concentration of potassium, high in uranium and thorium. This region was observed to be characterized by low magnetic (in Fig. 2) and gravity (in Fig. 5(b)) signatures. Potassium depletion relative to high eU and eTh could be due to weathering, as K is the radioelement that is mostly affected by weathering processes (Dickson and Scott, 1997). **GR4** also corresponds with the belt-type granitoids, characterized by considerable amount of potassium, thorium and uranium within the study area (Dzigbodi-Adjimah, 2004). The **MS** formation, characterized by metasedimentary rock was observed to show predominance in thorium and uranium against the depletion of potassium as shown in Figs. 6(d). The moderate to high in K region (shown as **MV1** in Fig. 6(a)) corresponds with the Birimian metavolcanic terrane. This appreciable concentration of K within the metavolcanic formation is associated with surface soils in K altered volcanic terranes, which exhibit high concentration in K, moderate concentration in eU and eTh than the underlying weathered

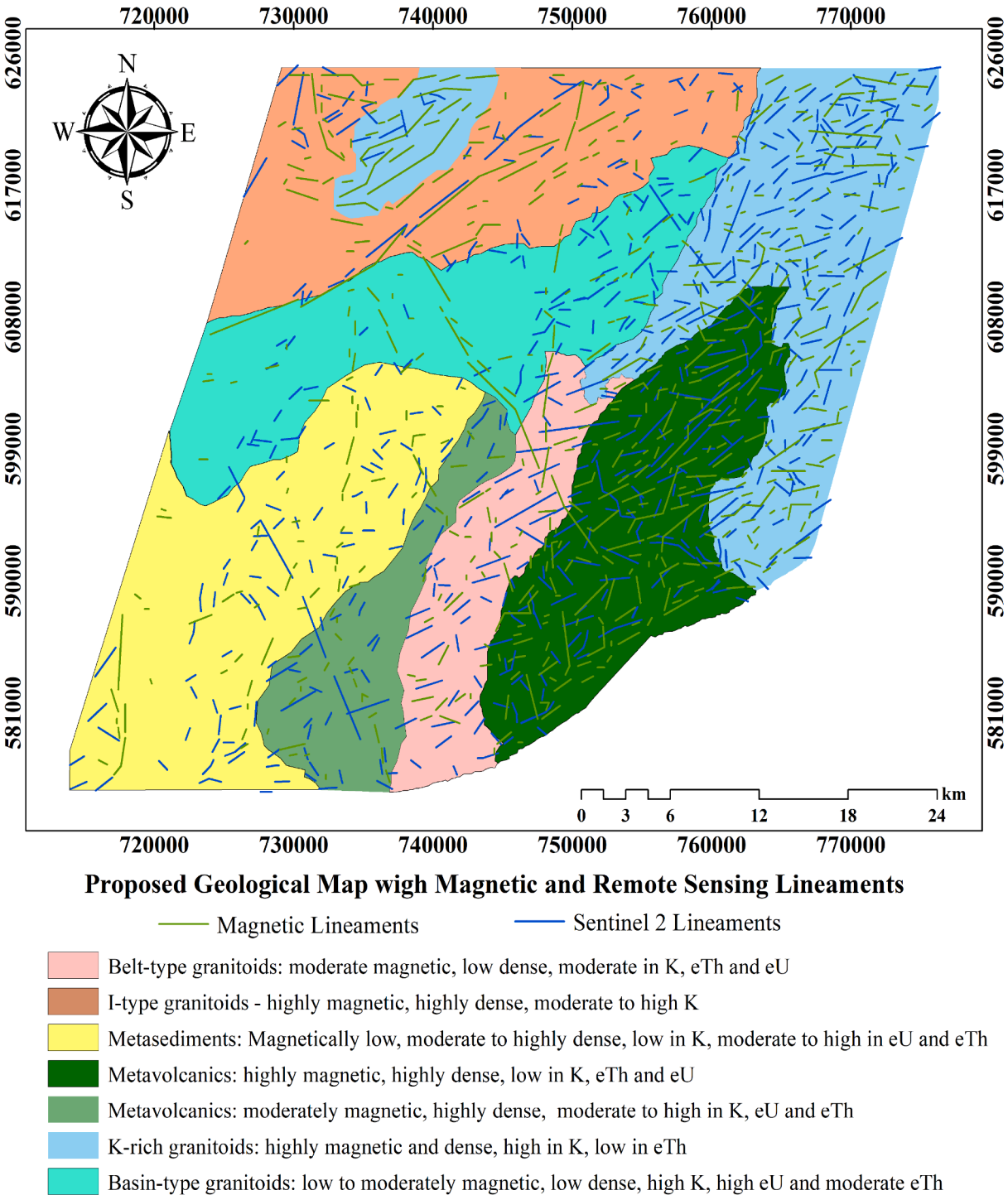

Fig. 10. Proposed geological map of the southern Kibi-Winneba belt with major integrated structures from magnetic and remote sensing.

rock (Dickson and Scott, 1997).

4.4. Sentinel 2A results

4.4.1. Principal Component Analysis (PCA)

It is observed that, 55.9914% of the total variance is contributed by the eigenvalue obtained for principal component 1 (PC1), with PC2 to PC4 showing a declined values in variance as shown in Table 2. This decline in variance by the PC2, PC3 and PC4 is due to differences in spectral regions as well as each band (Ranjbar et al., 2004; Liu et al., 2011).

Scrutinizing the eigenvector results of the PCA loadings of selected bands 2, 8, 11 and 12 demonstrated a clear contrast between band 11 (0.62108) and band 12 (-0.70417) within principal component 4 (PC4) as shown in Table 2. This PC4 values observed primarily show hydroxyl minerals as dark pixels and hence PC4 was negated to show the bright (white) pixel regions as hydroxyl minerals within the study area. This subsequently allowed for the delineation of hydroxyl associated minerals within the study area, whose image is shown in Fig. 7(a) (OH image). These regions of predominance in hydroxyl associated mineralized alteration are highlighted in bright pixels within the study area. Results from PCA for iron bearing minerals obtained in Table 3 for PC1,

Table 5
Weight of evidential layers and their respective class ranks.

Spatial Layers	Weight	Normalized Class	Class Score
Structural Density	25	0.0–0.2	1
		0.2–0.4	2
		0.4–0.7	3
		0.7–0.1	4
Magnetic Anomaly	24	0.0–0.2	1
		0.2–0.4	2
		0.4–0.7	3
		0.7–0.1	4
Gravity Anomaly	13	0.0–0.2	1
		0.2–0.4	2
		0.4–0.7	3
		0.7–0.1	4
Potassium Alteration	18	0.0–0.2	1
		0.2–0.4	2
		0.4–0.7	3
		0.7–0.1	4
Fe and OH Alteration	20	0.0–0.2	1
		0.2–0.4	2
		0.4–0.7	3
		0.7–0.1	4

PC2, PC3 and PC4 contributed to 56.7515%, 37.2616%, 5.7458% and 0.2411% respectively of the total variance. Bands 2 and 4 of PC1 and PC3 all have positive signs and are not recommended since it doesn't show any distinction between the reflectances of visible blue (band 2) and visible red (band 4) bands. PC4 was more preferred because, it showed a distinction between band 2 (0.69826) and band 4 (-0.69713), with these bands subsequently showing higher loadings. This clear distinction between bands 2 and 4 showing high and low reflectances respectively was due to the positive and negative eigenvector values associated with them and hence displays the iron pixels originally as dark pixel. In view of this, PC4 was negated to generate bright pixels which emphasize regions predominated by iron oxide minerals within the study area shown in Fig. 7 (Fe image). These two images obtained in Fig. 7(a) and (b) representing respectively delineated hydroxyl bearing minerals as well as iron bearing minerals were combined to produced an image shown in Fig. 7(c) known as OH + Fe image. A false colour composite (FCC) map was subsequently generated by assigning the OH image, Fe image, OH + Fe image to red, green and blue respectively to produce a map shown in Fig. 7(d). Regions showing green on the FCC (in Fig. 7) depicts hydrothermal alteration zones rich in goethite, amphibolite, argillite, sericite and ilmenite minerals known to characterize mesothermal quartz-vein gold deposits as well as the sulphide dominant regions (Klemd et al., 2002; Ranjbar et al., 2004).

4.4.2. Extracted lineaments and structural density maps for sentinel 2A data

The lineaments (in Fig. 8(a)) and lineament density (in Fig. 8(b)) delineated from the remote sensing data are nearly synonymous to the lineaments and lineaments density maps (Fig. 4(a) and Fig. 4(b)) generated from the aeromagnetic data. It can be observed that the highly fractured (densed) regions characterize regions delineated as highly magnetic (Figs. 2(b) and (c)), highly anomalous in gravity (Fig. 5(b)), highly anomalous in potassium (Fig. 6(a)) as well as high region of iron and hydroxyl alteration (**GR1**) (in Fig. 7(d)) was also observed to be of high structural density on the structural lineament (Fig. 8) and structural density (Fig. 8(b)) maps obtained from the remote sensing data.

4.5. Trends of delineated lineaments within the southern Kibi-Winneba belt

Gold mineralization within mesothermally quartz-vein deposits is controlled by structural features. The structural lineaments extracted from the magnetic and remote sensing datasets respectively in Figs. 9(a) and 9(b) indicated that, approximately 72% and 67% of lineaments obtained were oriented in the NE-SW (northeast-southwest) and N-S (north–south) directions. The N-S and NE-SW corroborates respectively the occurrence of D1 and D6 deformational and mineralizing events, which are the favourable structural orientations associated gold mineralization within the study area (Perrouty et al., 2012).

4.6. Proposed geological and structural map of the southern Kibi-Winneba belt

Magnetic, gravity and radiometric signatures corroborated by regional scale geological map of the southern Kibi-Winneba belt were employed to produce a geological map for the study area (in Fig. 10). A highly magnetic, more dense region with highly prevalent potassic alteration correlated with the Birimian granitoids with granodiorite prevalence in the eastern and northwestern part of the study area (Klemd et al., 2002; Anum et al., 2015; Tetteh and Effisah-Otoo, 2017). The highly magnetic and gravity signatures coupled with low response from all the three radioelements correlated with the highly mafic Birimian metavolcanic formation. Another metavolcanic formation was delineated as moderately magnetic, highly dense with moderate to high concentration in K. Fairly high K concentration in the metavolcanic terrane characterizes surface soil inferences overlain the weathered metavolcanic formation (Dickson and Scott, 1997). The moderately to highly dense and low magnetic signatures coupled with low eU and moderate to high eTh and K signatures also correlated with the Birimian metasediments. Magnetic, gravity and radiometric signatures corroborated by regional scale geological map of the southern Kibi-Winneba belt were employed to produce a geological map for the study area (in Fig. 10). The highly magnetic and gravity signatures coupled with low response from all the three radioelements correlated with the highly mafic Birimian metavolcanic formation. Another metavolcanic formation was delineated as moderately magnetic, highly dense with moderate to high concentration in K. Fairly high K concentration in the metavolcanic terrane characterizes surface soil inferences overlain the weathered metavolcanic formation (Dickson and Scott, 1997). The moderately to highly dense and low magnetic signatures coupled with low eU and moderate to high eTh and K signatures also correlated with the Birimian metasediments. A low magnetic and gravity responses coupled with relatively high radiometric responses correlated with the basin type granitoids. The magnetically low and lowly dense regions, delineated between the metavolcanics corroborated with the belt type granitoids (Dzigbodi-Adjimah, 2004). Also, the highly magnetic, moderately dense, moderate to high potassium concentrated region with high structural density occurrence has been delineated as I-type (Igneous type) granitoid terrane, characterized by possible prevalence of oxide and hornblende associated minerals such as magnetite and amphibolite (Chappell and White, 1992; Frost et al., 2001; Klemd et al., 2002; Nyarko et al., 2012). In thermally active regions, such as the southern Kibi-Winneba belt, possible occurrence of mineral alteration accompanied with the invasion of hydroxyl and iron bearing minerals are evident (Klemd et al., 2002). In view of this, hydroxyl and iron alteration zones delineated based on the Crosta Technique also depicted significant pathfinders to gold mineralization in the study area. These alteration zones delineated alteration zones of hydroxyl and iron associated minerals such as amphibolite, pyrrhotite, argillite, ilmenite and sericite which are more characteristic to mesothermally quartz vein deposits. These regions of iron and hydroxyl bearing minerals coincided with considerable regions within the highly fractured regions, metasediments, metavolcanics and the potassic alteration zone.

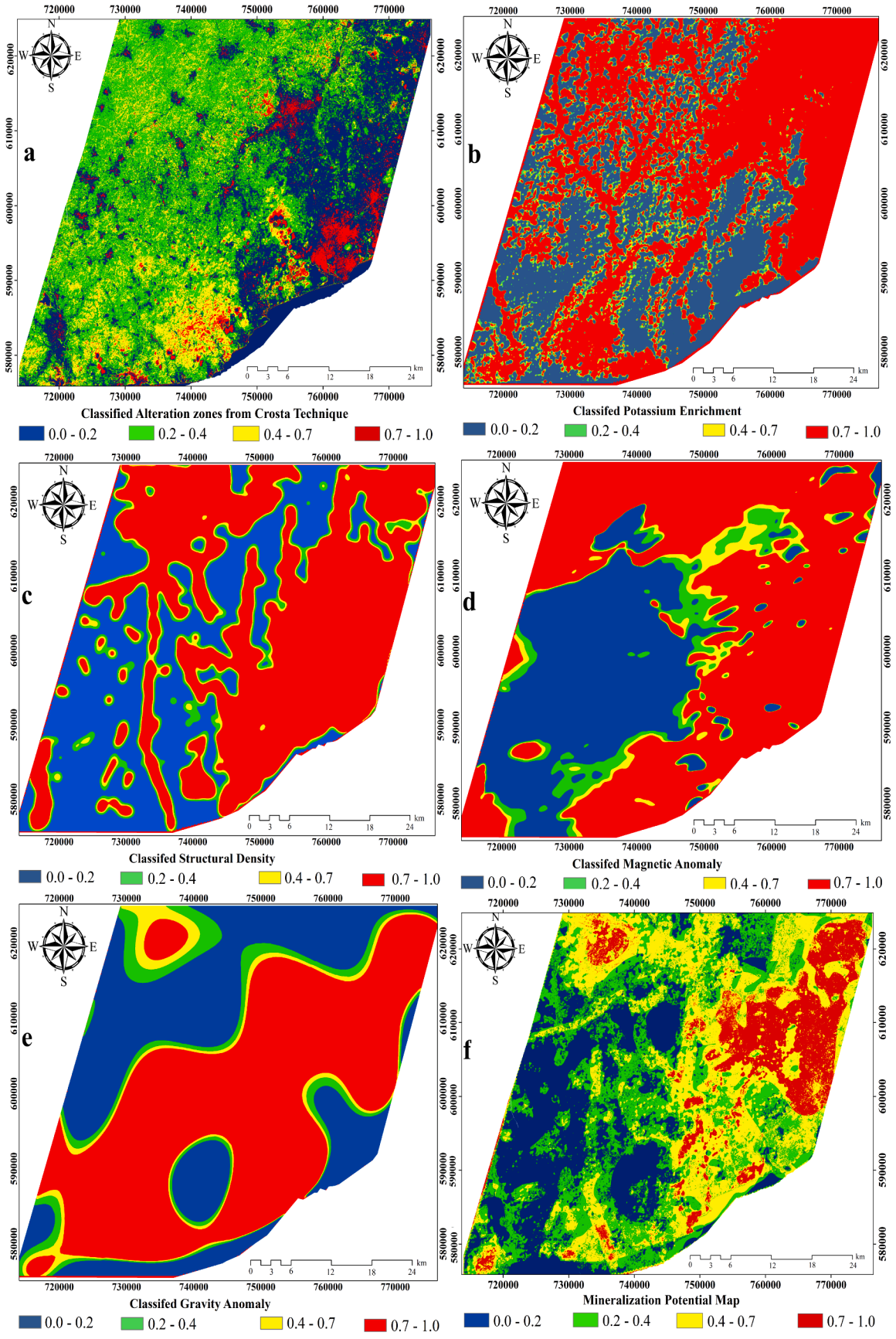

Fig. 11. (a) Classified alteration map based on Crosta technique (b) Classified K map (c) Classified Structural density map (d) Classified magnetic anomaly map (e) Classified gravity map (f) Mineral potential map (MPM).

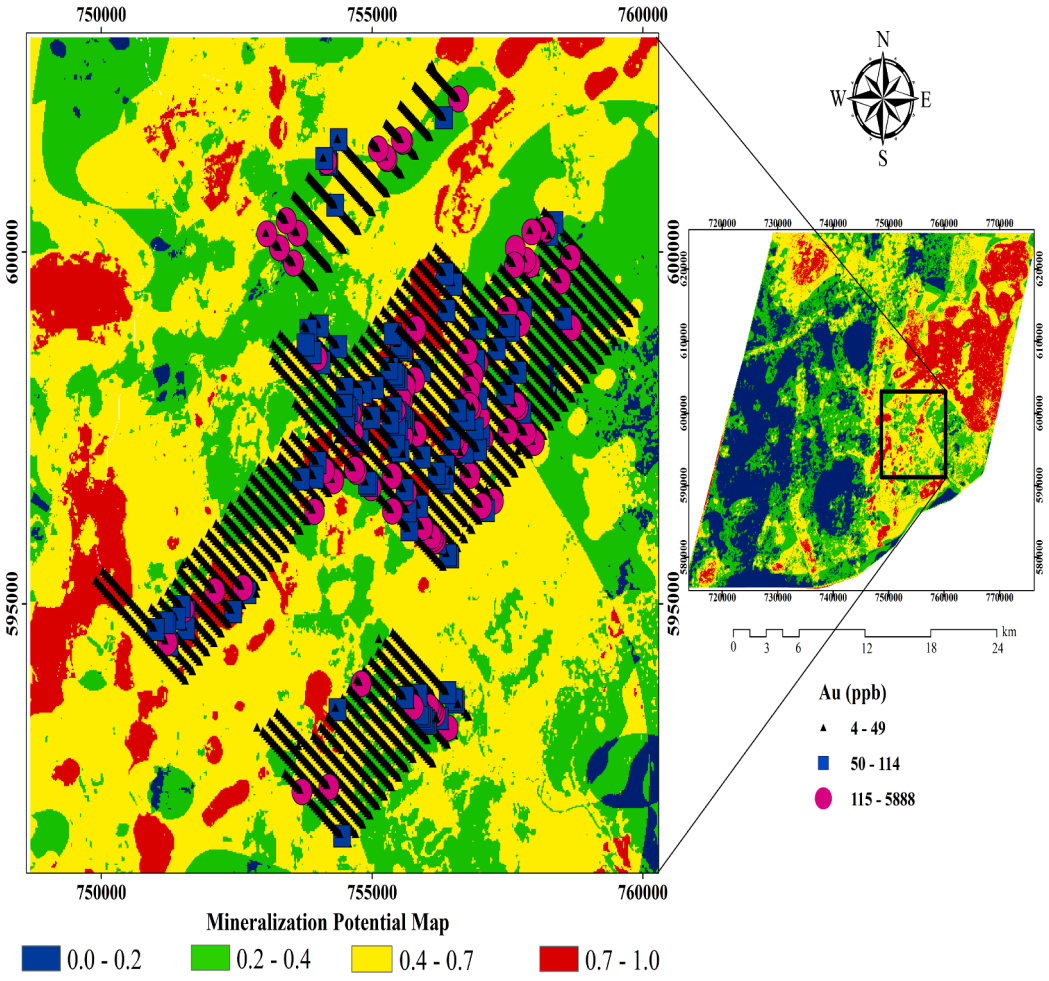

Fig. 12. Available data of gold in soil values superimposed on the mineral potential map of the southern Kibi-Winneba belt.

5. Discussion

5.1. Integration of exploration datasets

In order to produce a potential map depicting regions of gold mineralization within the southern Kibi-Winneba belt, several evidential layers encompassing hydrothermal alteration map from the Sentinel 2A, structural density map from CET analysis, magnetic anomaly, gravity anomaly and potassium alteration maps were integrated based on weighted overlay in ArcGIS. Each of these evidential layers was normalized based on Eq. 1 to range of values from 0 to 1. The assignment of weight based on weighted overlay shown in Table 5 was carried out in accordance with the relevance of the layer to gold mineralization within the southern Kibi-Winneba belt. In general, each of these five evidential layers gave an indication of gold mineralization potential within the study area (Klemd et al., 2002; Forson et al., 2020). It is however noteworthy that, their relevance to gold mineralization within the study area are not the same. Structural density characterizes regions of low pressure with the capability of hosting hydrothermal fluids with traces of gold mineralization (shown in Fig. 11(b)). The magnetic anomaly layer (shown in Fig. 11(d)) depicts regions within the study area associated with the occurrence of minerals dominated by arsenopyrite and magnetite, which are subsequently relevance to gold mineralization within the southern Kibi-Winneba belt. The gravity anomaly layer (shown in Fig. 11(c)) delineates the presence of bulk mineral deposits associated with mafic minerals such as pyrite and arsenopyrite, which are associated with gold mineralization within the study area. The potassium alteration layer (shown in Fig. 11(e)) as well as the iron and hydroxyl layer (shown in Fig. 11(a)) obtained from Crosta technique depicts regions of potassic, sericite and argillite bearing minerals which connote the occurrence of gold mineralization within the study area (Klemd et al., 2002; Forson et al., 2020). These descriptions of each of these evidential was significant in their respectively assigned weight which was vital in the generation in mineral potential map shown in Fig. 11(f). Each of these five evidential layers was then featured into four classes and assigned their respective scores and weights as shown in Table 5. The mineral potential map produced for the southern Kibi-Winneba belt in Fig. 11(f) was normalized based on Eq. 1 and was subsequently classified into four ranges (i.e. 0.0–0.2, 0.2–0.4, 0.4–0.7 and 0.7–1.0 depicting regions of low, moderately low, moderately high and high mineral potential respectively). This mineral potential map (shown in Fig. 11(f)) classifies 295.20km^2, which represents 13.34% of the belt as a highly potential region (with a prospectivity score of 0.7 to 1.0) for gold mineralization. This region is predominantly observed in the eastern part of the belt within the granitoids and the Birimian metavolcanics as well as the northwestern part of the study area within the granitoids. The moderately high regions, with prospectivity score of 0.4 to 0.7 of gold mineralization are observed predominantly within the northern, eastern and the southern part of the study with an area coverage of 635.95km^2 (representing 28.74% of the study area). An area coverage of 681.27km^2, representing 30.79% of the study area was classified to be a region of moderately low mineralization potential with a prospectivity score of 0.2 to 0.4. These moderately low regions are predominantly observed in the northern and central parts of the study area. 27.13% of the study area, representing 600.4km^2 of the belt (observed majorly in the central and western part of the belt) is

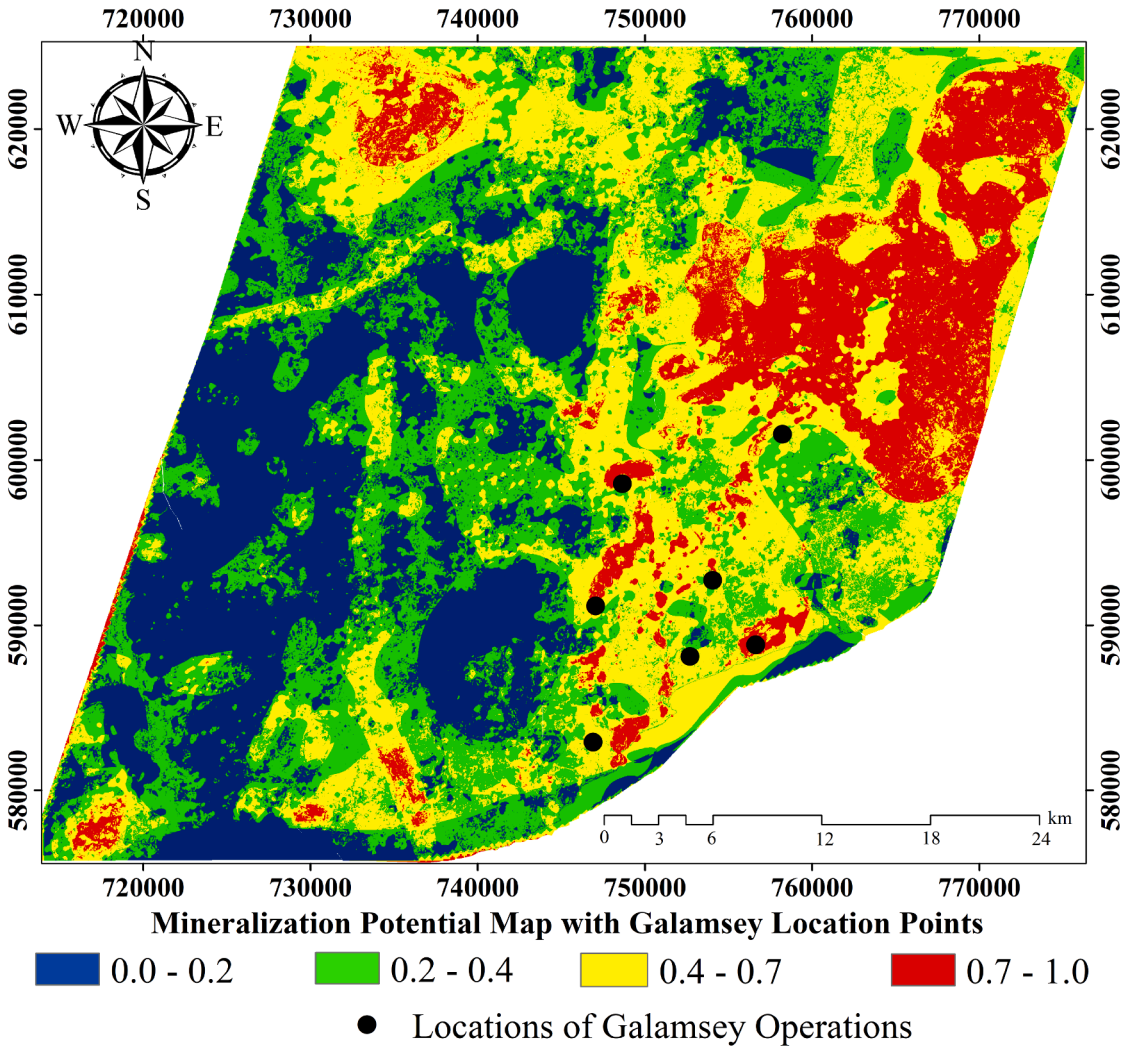

Fig. 13. Mineral potential map of the southern Kibi-Winneba belt showing sites of artisinal mining operations with black dots.

considered to be lowly prospective for gold mineralization with a prospectivity score below 0.2.

5.2. Validation of mineral potential map by geochemical data

Available geochemical datasets of gold in soil assay values in the eastern part (within the metavolcanics) of the study area were employed to validate the mineral potential map produced as shown in Fig. 12. The moderate to highly prospective regions of gold mineralization occurrences delineated within that enclave also corroborated by the site locations of artisinal mining activities (in Fig. 13).

5.3. Relating artisanal mining sites with the Mineral Potential Map

Sites of previously abandoned and ongoing operations in recent years by artisanal gold miners were superimposed on the MPM (in Fig. 13). These Galamsey operation points corroborated with the highly prospective zones of gold mineralization, delineated on the MPM (Fig. 11 (f)). Images from field observations (Fig. 14(a), 14(b), 14(c) and 14(d)) within trenches around the areas of galamsey operations revealed the occurrence of foliations in rocks as well as the presence of fold-like structures within the gold bearing quartz-veins within the Birimian metavolcanics. Quartz-schists that comprises various oxide and sulphide minerals associated with gold mineralization were also found.

6. Conclusion

The spatial relationship between lithological units, structural lineaments as well as alteration zones have been delineated by employing geophysical and remote sensing datasets encompassing magnetic, gravity, radiometric and Sentinel 2A within the southern Kibi-Winneba belt. A geological map for the study area, generated from the geophysical, remote sensing and geological datasets delineated lithological formations encompassing Belt-type granitoids, K-rich granitoids, I-type granitoids, Basin-type granitoids, Birimian metasediments and metavolcanics. Approximately 72% and 67% structural lineaments delineated respectively from the magnetic and Sentinel 2A datasets trended in the NE-SW and N-S direction (which are the lineament directional trends that control gold mineralization in the study area) representing respectively the D6 and D1 deformation and mineralization events. The application of PCA based on Crosta technique was vital in highlighting alteration zones related to gold mineralization within the southern Kibi-Winneba belt. The mineralization potential of the study area was also highlighted by integrating magnetic anomaly, gravity anomaly, structural density, potassium concentration and Iron and clay alteration layers based on weighted overlay technique in a geographic information system (GIS). Four zones were delineated within the southern Kibi-Winneba belt, representing respectively 27.13%, 30.79%, 28.74% and 13.34% as low, moderately low, moderately high and highly prospective regions of gold mineralization within the belt. Available gold in soil

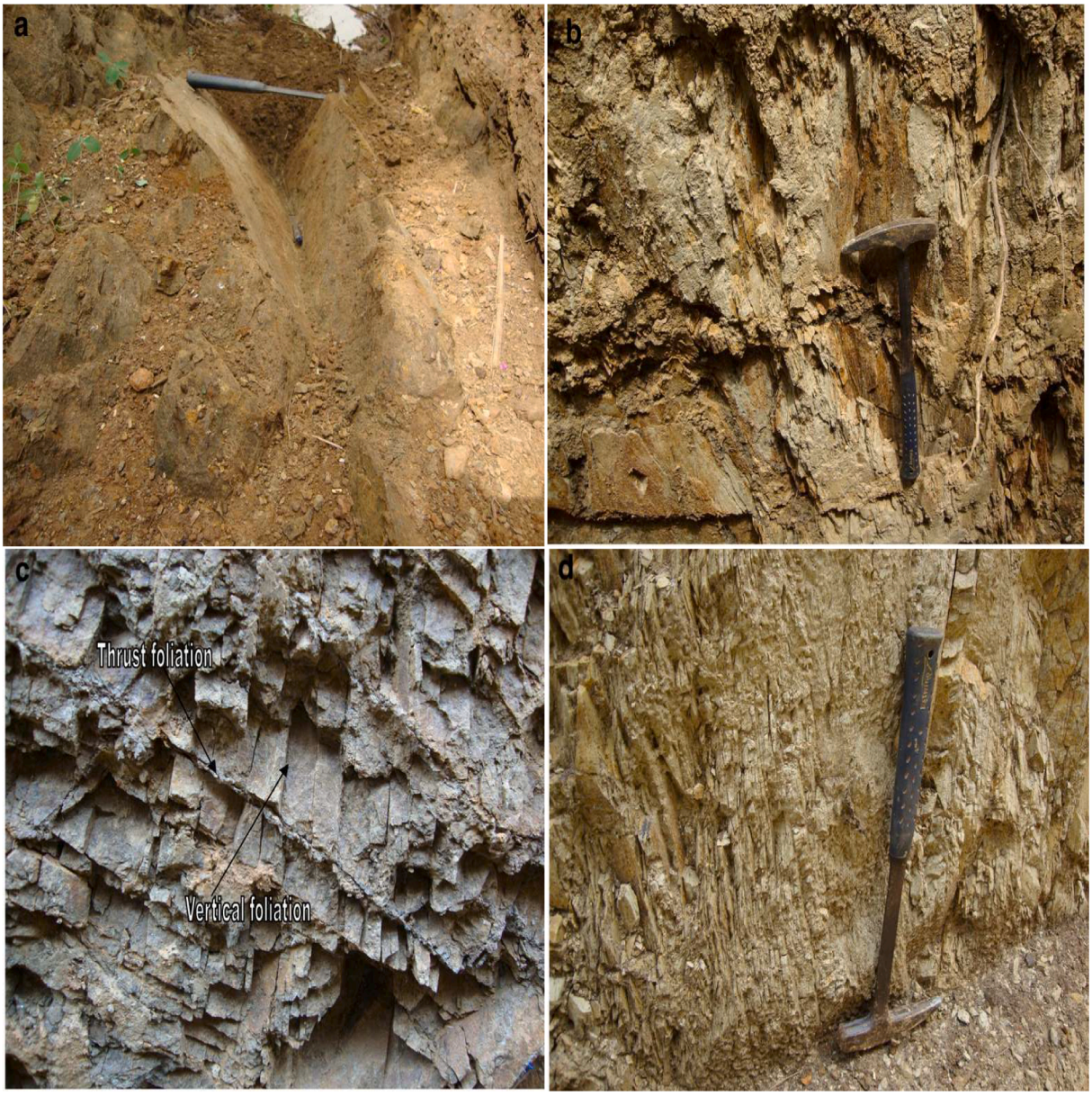

Fig. 14. (a) Fold-like structure due to crossed foliations (b) Sub-vertical foliation in schists (c) Vertical parallel planar foliation (surfaces) cut across by sub-horizontal east dipping thrust foliation (d) Vertical shear foliation in quartz-muscovite schist.

assay results and locations of artisanal mining operations (Galamsey) corroborated with the delineated highly potential mineralization zones of gold deposits within the study area. In view of this, the integration of geophysical, remote sensing coupled with geological and geochemical datasets have been vital in delineating the potential zones of gold mineralization occurrences within the southern Kibi-Winneba belt. Thus, the gold mineralization potential map generated can be employed as a preliminary reference in selecting sites for gold exploration. It is ideated that the results obtained for the mineral alteration and potential zones as well as the proposed geological map would be an essential guide to various future surveys intended to unravel the prospectivity of the southern Kibi-Winneba belt and hence these techniques employed would be essential in delineation of lithologies, structural lineaments and alteration zones in other geological terranes.

Declaration of Competing Interest

The authors declare that they have no known competing financial interests or personal relationships that could have appeared to influence the work reported in this paper.

Acknowledgements

Authors wish to thank Ghana Geological Survey Authority, GFZ German Research Centre for Geoscience and the United States Geological Survey Earth Resources Observation and Science Center (USGS-EROS) for making data available for the research.

References

Abdullah, A., Akhir, J.M., Abdullah, I., 2010. Automatic mapping of lineaments using shaded relief images derived from digital elevation model (dems) in the maran–sungi lembing area, malaysia. Electron. J. Geotech. Eng. 15 (6), 949–958.

Abuzied, S.M., Ibrahim, S.K., Kaiser, M.F., Seleem, T.A., 2016. Application of remote sensing and spatial data integrations for mapping porphyry copper zones in nuweiba area, egypt. Int. J. Signal Process. Syst. 4 (2), 102–108.

Adjovu, I., 2007. Exploration summary on the gomoa mangoase licence. Geodita Resources Ltd.

Ahmed, S., 2014. Lineament extraction from southern chitradurga schist belt using landsat tm, astergdem and geomatics techniques. Int. J. Computer Appl. 93 (12).
Airo, M.-L. (2015). Geophysical signatures of mineral deposit types in Finland. Geological survey of Finland.
Amenyoh, T., Wemegah, D., Menyeh, A., Danuor, S., 2009. The use of landsat and aeromagnetic data in the interpretation of geological structures in the nangodi belt. In: Proc of the 26th Biennial Conference of the Ghana Science Association, volume 4. University. of Capecoast.
Anum, S., Sakyi, P.A., Su, B.-X., Nude, P.M., Nyame, F., Asiedu, D., Kwayisi, D., 2015. Geochemistry and geochronology of granitoids in the kibi-asamankese area of the kibi-winneba volcanic belt, southern ghana. J. Afr. Earth Sc. 102, 166–179.
Beiranvand Pour, A., Park, T.-Y.S., Park, Y., Hong, J.K., Zoheir, B., Pradhan, B., Ayoobi, I., Hashim, M., 2018. Application of multi-sensor satellite data for exploration of zn–pb sulfide mineralization in the franklinian basin, north greenland. Remote Sensing 10 (8), 1186.
Beiranvand Pour, A., Park, Y., Crispini, L., Läufer, A., Kuk Hong, J., Park, T.-Y.S., Zoheir, B., Pradhan, B., Muslim, A.M., Hossain, M.S., et al., 2019a. Mapping listvenite occurrences in the damage zones of northern victoria land, antarctica using aster satellite remote sensing data. Remote Sensing 11 (12), 1408.
Beiranvand Pour, A., S Park, T.-Y., Park, Y., Hong, J.K., M Muslim, A., Läufer, A., Crispini, L., Pradhan, B., Zoheir, B., Rahmani, O., et al. (2019b). Landsat-8, advanced spaceborne thermal emission and reflection radiometer, and worldview-3 multispectral satellite imagery for prospecting copper-gold mineralization in the northeastern inglefield mobile belt (imb), northwest greenland. Remote Sensing, 11 (20):2430.
Beygi, S., Talovina, I.V., Tadayon, M., Pour, A.B., 2020. Alteration and structural features mapping in kacho-mesqal zone, central iran using aster remote sensing data for porphyry copper exploration. Int. J. Image Data Fusion 1–21.
Blakely, R.J., 1995. Potential theory in gravity and magnetic applications. Cambridge University Press.
Blakely, R.J., Simpson, R.W., 1986. Approximating edges of sources bodies from magnetic or gravity anomalies. Geophysics 51 (7), 1494–1498.
Boadi, S., Nsor, C.A., Antobre, O.O., Acquah, E., 2016. An analysis of illegal mining on the offin shelterbelt forest reserve, ghana: Implications on community livelihood. J. Sustainable Mining 15 (3), 115–119.
Boateng, D.O., Nana, F., Codjoe, Y., Ofori, J., 2014. Impact of illegal small scale mining (galamsey) on cocoa production in atiwa district of ghana. Int. J. Adv. Agric. Res. 2, 89–99.
Bolouki, S.M., Ramazi, H.R., Maghsoudi, A., Beiranvand Pour, A., Sohrabi, G., 2020. A remote sensing-based application of bayesian networks for epithermal gold potential mapping in ahar-arasbaran area, nw iran. Remote Sensing 12 (1), 105.
Brempong, F., Wemegah, D.D., Preko, K., Armah, T., Boadi, B., Menyeh, A., Oppong, I.A., Quarshie, M.M., Aning, A.A., Asare, V.S., et al., 2019. Interpretation of geological structures hosting potential gold deposits in the konongo gold mine using airborne magnetic, electromagnetic and radiometric datasets. J. Geosci. Environ. Protection 7 (6), 203–225.
Chappell, B.W., White, A., 1992. I-and s-type granites in the lachlan fold belt. Earth Environ. Sci. Trans. R. Soc. Edinburgh 83 (1–2), 1–26.
Clark, D.A., 1999. Magnetic petrology of igneous intrusions: implications for exploration and magnetic interpretation. Explor. Geophys. 30 (2), 5–26.
Dehnavi, A.G., Sarikhani, R., Nagaraju, D., 2010. Image processing and analysis of mapping alteration zones in environmental research, east of kurdistan, iran. World Appl. Sci. J. 11 (3), 278–283.
Dentith, M., Mudge, T.S., 2014. Geophysics for the mineral exploration geoscientist. Cambridge University Press.
Dickson, B., Scott, K., 1997. Interpretation of aerial gamma-ray surveys-adding the geochemical factors. J. Aust. Geol. Geophys. 17, 187–200.
Dove, K., 1991. Geology of the $I = 4$ field sheets nos. 29 and 31, Winneba SW and NW. Archive Report 25. Ghana Geological Survey Department. Accra.
Dransfield, M.H., Buckingham, M., Van Kann, F., 1994. Lithological mapping by correlating magnetic and gravity gradient airborne measurements. Explor. Geophys. 25 (1/2), 25–30.
Dufrechou, G., Harris, L., Corriveau, L., Antonoff, V., 2015. Regional and local controls on mineralization and pluton emplacement in the bondy gneiss complex, grenville province, canada interpreted from aeromagnetic and gravity data. J. Appl. Geophys. 116, 192–205.
Dzigbodi-Adjimah, K., 2004. The mineralogy and petrography of the ferruginous manganese rocks at mankwadzi, ghana. J. Afr. Earth Sc. 38, 293–315.
Eisenlohr, B., 1989. The structural geology of Birimian and Tarkwaian rocks of southwest Ghana: Republic of Ghana, Federal Republic of Germany, Technical Cooperation Project no. 80.2040. 6. BGR.
Eisenlohr, B., Hirdes, W., 1992. The structural development of the early proterozoic birimian and tarkwaian rocks of southwest ghana, west africa. J. African Earth Sci. (Middle East) 14 (3), 313–325.
Fairhead, J.D., Cooper, G., Sander, S., Tschirhart, V., Thomas, M., 2017. Advances in airborne gravity and magnetics. Proc. Exploration 17, 113–127.
Forson, E.D., Menyeh, A., Wemegah, D.D., Danuor, S.K., Adjovu, I., Appiah, I., 2020. Mesothermal gold prospectivity mapping of the southern kibi-winneba belt of ghana based on fuzzy analytical hierarchy process, concentration-area (c-a) fractal model and prediction-area (p-a) plot. J. Geophys. 174 (103971).
Frost, B.R., Barnes, C.G., Collins, W.J., Arculus, R.J., Ellis, D.J., Frost, C.D., 2001. A geochemical classification for granitic rocks. J. Petrology 42 (11), 2033–2048.
Frutuoso, R., Lima, A., Teodoro, A.C., 2021. Application of remote sensing data in gold exploration: targeting hydrothermal alteration using landsat 8 imagery in northern portugal. Arabian J. Geosci. 14 (6), 1–18.
Goetz, A.F.H., Roman, L.C., 1981. Geologic Remote Sensing 211, 781–791.
Griffis, J.R., Barning, K., Agezo, L.F., Akosah, K.F., 2002. Gold deposits of ghana. In: Graphic Evolution Ltd. Minerals Commission of Ghana, Ontario, Canada.
Hilson, G., Hilson, C.J., Pardie, S., 2007. Improving awareness of mercury pollution in small-scale gold mining communities: challenges and ways forward in rural ghana. Environ. Res. 103 (2), 275–287.
Hinze, W.J., Von Frese, R.R., Saad, A.H., 2013. Gravity and magnetic exploration: Principles, practices, and applications. Cambridge University Press.
Holden, E.-J., Fu, S.C., Kovesi, P., Dentith, M., Bourne, B., Hope, M., 2011. Automatic identification of responses from porphyry intrusive systems within magnetic data using image analysis. J. Appl. Geophys. 74 (4), 255–262.
Jorgensen, G.J., Kisabeth, J.L., Huffman, A.R., 2002. Method for integrating gravity and magnetic inversion with geopressure prediction for oil, gas and mineral exploration and production. US Patent 6,430,507.
Kamguia, J., Manguelle-Dicoum, E., Tabod, C., Tadjou, J., 2005. Geological models deduced from gravity data in the garoua basin, cameroon. J. Geophys. Eng. 2 (2), 147–152.
Kessey, K.D., Arko, B., 2013. Small scale gold mining and environmental degradation, in ghana: issues of mining policy implementation and challenges. J. Stud. Social Sci. 5 (1).
Klemd, R., Hünken, U., Olesch, M., 2002. Metamorphism of the country rocks hosting gold–sulfide-bearing quartz veins in the paleoproterozoic southern kibi-winneba belt (se-ghana). J. Afr. Earth Sc. 35 (2), 199–211.
Kocal, A., Duzgun, H., Karpuz, C., 2004. Discontinuity mapping with automatic lineament extraction from high resolution satellite imagery. ISPRS XX, Istanbul, pages 12–23.
Kovesi, P., et al., 1997. Symmetry and asymmetry from local phase. In: Tenth Australian joint conference on artificial intelligence, volume 190. Citeseer, pp. 2–4.
Leube, A., Hirdes, W., Mauer, R., Kesse, G.O., 1990. The early proterozoic birimian supergroup of ghana and some aspects of its associated gold mineralization. Precambr. Res. 46 (1–2), 139–165.
Liang, S., Sun, S., Lu, H., 2021. Application of airborne electromagnetics and magnetics for mineral exploration in the baishiquan–hongliujing area, northwest china. Remote Sensing 13 (5), 903.
Liu, L., Zhuang, D.-F., Zhou, J., Qiu, D.-S., 2011. Alteration mineral mapping using masking and crosta technique for mineral exploration in mid-vegetated areas: a case study in areletuobie, xinjiang (china). Int. J. Remote Sens. 32 (7), 1931–1944.
Magiera, J., 2018. Can satellite remote sensing be applied in geological mapping in tropics?. In: E3S Web of Conferences, volume 35 EDP Sciences, p. 02004.
Malehmir, A., Dynesius, L., Paulusson, K., Paulusson, A., Johansson, H., Bastani, M., Wedmark, M., Marsden, P., 2017. The potential of rotary-wing uav-based magnetic surveys for mineral exploration: A case study from central sweden. Lead. Edge 36 (7), 552–557.
McKinley, J., Deutscht, C., Neufeldt, C., Patton, M., Cooper, M., Young, M., 2014. Use of geostatistical bayesian updating to integrate airborne radiometrics and soil geochemistry to improve mapping for mineral exploration. J. South Afr. Inst. Min. Metall. 114 (8), 575.
Moradpour, H., Rostami Paydar, G., Pour, A.B., Valizadeh Kamran, K., Feizizadeh, B., Muslim, A.M., Hossain, M.S., 2020. Landsat-7 and aster remote sensing satellite imagery for identification of iron skarn mineralization in metamorphic regions. Geocarto Int. 1–28.
Newmont, 2006. Terminal report on gomoa prospecting license (pl3/66). Newmont Ghana Gold Limited.
Nyarko, E., Aseidu, D., Osea, S., Dampare, S., Zakaria, N., Hanson, J., Osei, J., Enti-Brown, S., Tulasi, D., 2012. Geochemical characteristics of the basin-type granitoids in the winneba area of ghana. Proc. Int. Acad. Ecol. Environ. Sci. 2 (3), 177.
Nykänen, V., Salmirinne, H., 2007. Prospectivity analysis of gold using regional geophysical and geochemical data from the central lapland greenstone belt, finland. Geological Survey Finland 44, 251–269.
Ontoyin, J., Agyemang, I., 2014. Environmental and rural livelihoods implications of small-scale gold mining in talensi-nabdam districts in northern ghana. J. Geography Regional Planning 7 (8), 150–159.
Oruç, B., Selim, H., 2011. Interpretation of magnetic data in the sinop area of mid black sea, turkey, using tilt derivative, euler deconvolution, and discrete wavelet transform. J. Appl. Geophys. 74 (4), 194–204.
Ostrovskiy, E.Y., 1975. Antagonism of radioactive elements in wallrock alterations fields and its use in aerogamma spectrometric prospecting. Int. Geolog. Rev. 17, 461–468.
Perrouty, S., Aillères, L., Jessell, M.W., Baratoux, L., Bourassa, Y., Crawford, B., 2012. Revised eburnean geodynamic evolution of the gold-rich southern ashanti belt, ghana, with new field and geophysical evidence of pre-tarkwaian deformations. Precambr. Res. 204, 12–39.
Pinet, N., Gloaguen, E., Giroux, B., 2019. Introduction to the special issue on geophysics applied to mineral exploration. Can. J. Earth Sci. 56(5):v–viii.
Pour, A.B., Ali, A., 2014. Lithological mapping and hydrothermal alteration using landsat 8 data: a case study in ariab mining district red sea hills sudan. Int. J. Basic Appl. Sci. 3 (3), 199–208.
Pour, A.B., Hashim, M., 2015. Hydrothermal alteration mapping from landsat-8 data, sar cheshmeh copper mining district, south-eastern islamic republic of iran. J. Taibah University Sci. 9 (2), 155–166.
Pour, A.B., Hashim, M., Hong, J.K., Park, Y., 2019. Lithological and alteration mineral mapping in poorly exposed lithologies using landsat-8 and aster satellite data: North-eastern graham land, antarctic peninsula. Ore Geol. Rev. 108, 112–133.
Pour, A.B., Park, Y., Park, T.-Y.S., Hong, J.K., Hashim, M., Woo, J., Ayoobi, I., 2019. Evaluation of ica and cem algorithms with landsat-8/aster data for geological mapping in inaccessible regions. Geocarto Int. 34 (7), 785–816.
Pour, A.B., Sekandari, M., Rahmani, O., Crispini, L., Läufer, A., Park, Y., Hong, J.K., Pradhan, B., Hashim, M., Hossain, M.S., et al., 2021a. Identification of phyllosilicates

in the antarctic environment using aster satellite data: Case study from the mesa range, campbell and priestley glaciers, northern victoria land. Remote Sensing 13 (1), 38.

Pour, A.B., Zoheir, B., Pradhan, B., and Hashim, M., 2021b. Editorial for the special issue: Multispectral and hyperspectral remote sensing data for mineral exploration and environmental monitoring of mined areas.

Ramadass, G., SubhashBabu, A., Laxmi, G.U., 2013. Structural analysis of airborne radiometric data for identification of kimberlites in parts of eastern dharwar craton. Int. J. Sci. Res. (IJSR).

Ramadass, G., SubhashBabu, A., Laxmi, G.U., 2015. Structural analysis of airborne radiometric data for identification of kimberlites in parts of eastern dharwar craton. Int. J. Sci. Res. 4 (4), 2375–2380.

Ramezanali, A., Mansouri, E., Feizi, F., 2017. Integration of aeromagnetic geophysical data with other exploration data layers based on fuzzy ahp and ca fractal model for cu-porphyry potential mapping: a case study in the fordo area, central iran. Bollettino di Geofisica Teorica ed Applicata 58 (1).

Ranjbar, H., Honarmand, M., Moezifar, Z., 2004. Application of the crosta technique for porphyry copper alteration mapping, using etm+ data in the southern part of the iranian volcanic sedimentary belt. J. Asian Earth Sci. 24 (2), 237–243.

Sabins, F.F., 1999. Remote sensing for mineral exploration. Ore Geol. Rev. 14 (3–4), 157–183.

Salehi, S., Mielke, C., Brogaard Pedersen, C., Dalsenni Olsen, S., 2019. Comparison of aster and sentinel-2 spaceborne datasets for geological mapping: a case study from north-east greenland. Geolog. Survey Denmark Greenland Bull. 43.

Schetselaar, E.M., Chung, C.-J.F., Kim, K.E., 2000. Integration of landsat tm, gamma-ray, magnetic, and field data to discriminate lithological units in vegetated. Remote Sens. Environ. 71 (1), 89–105.

Sekandari, M., Masoumi, I., Beiranvand Pour, A., M Muslim, A., Rahmani, O., Hashim, M., Zoheir, B., Pradhan, B., Misra, A., and Aminpour, S.M., 2020a. Application of landsat-8, sentinel-2, aster and worldview-3 spectral imagery for exploration of carbonate-hosted pb-zn deposits in the central iranian terrane (cit). Remote Sensing, 12(8):1239.

Sekandari, M., Masoumi, I., Pour, A.B., Muslim, A.M., Hossain, M.S., Misra, A., 2020b. Aster and worldview-3 satellite data for mapping lithology and alteration minerals associated with pb-zn mineralization. Geocarto Int. 1–31.

Senayah, J.K., Nketia, A.K., Gyansa, A.S., 2010. Report on the soil resources of gomoa east district, central region, ghana. Council for Scientific and Industrial Research (CSIR), Soil Research Institute CSIR/WAAPP NO. 017.

Shah, A.K., Bedrosian, P.A., Anderson, E.D., Kelley, K.D., Lang, J., 2013. Integrated geophysical imaging of a concealed mineral deposit: A case study of the world-class pebble porphyry deposit in southwestern alaska. Geophysics 78 (5), B317–B328.

Sheikhrahimi, A., Pour, A.B., Pradhan, B., Zoheir, B., 2019. Mapping hydrothermal alteration zones and lineaments associated with orogenic gold mineralization using aster data: A case study from the sanandaj-sirjan zone, iran. Adv. Space Res. 63 (10), 3315–3332.

Silva, A.M., Pires, A.C.B., Mccafferty, A., de Moraes, R.A.V., Xia, H., 2003. Application of airborne geophysical data to mineral exploration in the uneven exposed terrains of the rio das velhas greenstone belt. Brazilian J. Geol. 33 (2), 17–28.

Sobolev, I.S., Orekhov, A.N., Bratec, T., Rikhvanov, L.P., Soboleva, N.P., 2018. Variance-correlation analysis in the exploration of hydrothermal (fluidogenous) deposits using surface gamma-ray spectrometry. J. Appl. Geophys. 159, 597–604.

Tetteh, G., Effisah-Otoo, E., 2017. Petrography and geochemistry of some granitoids associated with gold mineralisation at mpohor area in southeastern ashanti belt of the birimian, ghana. Ghana Mining J. 17 (1), 31–42.

Thannoun, R.G., 2013. Automatic extraction and geospatial analysis of lineaments and their tectonic significance in some areas of northern iraq using remote sensing techniques and gis. International Journal Of Enhanced Research In Science Technology & Engineering Bulletin, 2.

Thomas, M.D., Pilkington, M., McCuaig, M., 2019. Evaluation of mineral exploration targets defined by airborne gravity gradiometry through gravity and magnetic modelling: vicinity of the iron range fault, purcell anticlinorium, southern canadian cordillera. Can. J. Earth Sci. 56 (5), 452–470.

Traore, M., Wambo, J.D.T., Ndepete, C.P., Tekin, S., Pour, A.B., Muslim, A.M., 2020. Lithological and alteration mineral mapping for alluvial gold exploration in the south east of birao area, central african republic using landsat-8 operational land imager (oli) data. J. Afr. Earth Sc. 170, 103933.

Walter, C., Braun, A., Fotopoulos, G., 2020. High-resolution unmanned aerial vehicle aeromagnetic surveys for mineral exploration targets. Geophys. Prospect. 68 (1), 334–349.

Wambo, J.D.T., Pour, A.B., Ganno, S., Asimow, P.D., Zoheir, B., dos Reis Salles, R., Nzenti, J.P., Pradhan, B., Muslim, A.M., 2020. Identifying high potential zones of gold mineralization in a sub-tropical region using landsat-8 and aster remote sensing data: A case study of the ngoura-colomines goldfield, eastern cameroon. Ore Geol. Rev. 122, 103530.

Wemegah, D.D., Preko, K., Noye, R.M., Boadi, B., Menyeh, A., Danuor, S.K., Amenyoh, T., 2015. Geophysical interpretation of possible gold mineralization zones in kyerano, south-western ghana using aeromagnetic and radiometric datasets. J. Geosci. Environ. Protection 3 (04), 67.

Xiao, Z., Hou, Z., Miao, C., Wang, J., 2005. Using phase information for symmetry detection. Pattern Recogn. Letters 26 (13), 1985–1994.

Yousefifar, S., Khakzad, A., Harooni, H.A., Karami, J., Jafari, M., Abedin, M.V., 2011. Prospecting of au and cu bearing targets by exploration data combination in southern part of dalli cu-au porphyry deposit, central iran. Arch. Min. Sci. 56 (1), 21–34.

Zoheir, B., El-Wahed, M.A., Pour, A.B., Abdelnasser, A., 2019. Orogenic gold in transpression and transtension zones: Field and remote sensing studies of the barramiya–mueilha sector, egypt. Remote Sensing 11 (18), 2122.